Brigham Young University
BYU ScholarsArchive

All Theses and Dissertations

2011-11-04

Microstructural Evaluation in Friction Stir Welded High Strength Low Alloy Steels

Majid Abbasi Gharacheh
Brigham Young University - Provo

Follow this and additional works at: https://scholarsarchive.byu.edu/etd

Part of the Mechanical Engineering Commons

BYU ScholarsArchive Citation

Abbasi Gharacheh, Majid, "Microstructural Evaluation in Friction Stir Welded High Strength Low Alloy Steels" (2011). *All Theses and Dissertations*. 3099.
https://scholarsarchive.byu.edu/etd/3099

This Dissertation is brought to you for free and open access by BYU ScholarsArchive. It has been accepted for inclusion in All Theses and Dissertations by an authorized administrator of BYU ScholarsArchive. For more information, please contact scholarsarchive@byu.edu, ellen_amatangelo@byu.edu.

Microstructural Evolution in Friction Stir Welded High Strength Low Alloy Steels

Majid Abbasi

A dissertation submitted to the faculty of
Brigham Young University
in partial fulfillment of the requirements for the degree of

Doctor of Philosophy

Tracy W. Nelson, Chair
Carl D. Sorensen
David T. Fullwood
Christopher Mattson
Anton Bowden
Mike Miles

Department of Mechanical Engineering

Brigham Young University

December 2011

Copyright © 2011 Majid Abbasi

All Rights Reserved

ABSTRACT

Microstructural Evolution in Friction Stir Welded High Strength Low Alloy Steels

Majid Abbasi
Department of Mechanical Engineering
Doctor of Philosophy

Understanding microstructural evolution in Friction Stir Welding (FSW) of steels is essential in order to understand and optimize the process. Ferritic steels undergo an allotropic phase transformation. This makes microstructural evolution study very challenging. An approach based on Electron Backscattered Diffraction (EBSD) and phase transformation orientation relationships is introduced to reconstruct pre-transformed grain structure and texture. Reconstructed pre-transformed and post-transformed grain structures and textures were investigated in order to understand microstructural evolution. Texture results show that there is evidence of shear deformation as well as recrystallization in the reconstructed prior austenite. Room temperature ferrite exhibits well-defined shear deformation texture components. Shear deformation texture in the room temperature microstructure implies that FSW imposes deformation during and after the phase transformation. Prior austenite grain boundary analysis shows that variant selection is governed by interfacial energy. Variants that have near ideal BCC/FCC misorientation relative to their neighboring austenite and near zero misorientation relative to neighboring ferrite are selected. Selection of coinciding variants in transformed prior austenite Σ3 boundaries supports the interfacial-energy-controlled variant selection mechanism.

Keywords: Majid Abbasi, Friction Stir Welding, HSLA, prior austenite reconstruction, phase transformation, texture, variant selection, sigma boundaries, grain boundary energy, misorientation

ACKNOWLEDGMENTS

I would like to begin with acknowledging the creator, the source of knowledge, and the ultimate engineer for the opportunity to discover and understand some behaviors of one the most abundant materials in this universe. Iron, an element that has benefited us humans with its unique properties for centuries. It is a very complex material that its formation, behaviors, and properties have not been fully understood despite the fact that it has been studied the most among all metallic materials. It is worth mentioning that one of the 114 chapters of Muslim’s holy book (Quran) is named after this element. Verse 25 in chapter 57 (Iron) states:

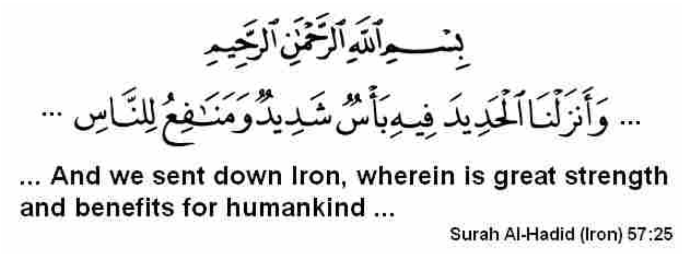

بِسْمِ ٱللَّهِ ٱلرَّحْمَٰنِ ٱلرَّحِيمِ

... وَأَنزَلْنَا ٱلْحَدِيدَ فِيهِ بَأْسٌ شَدِيدٌ وَمَنَٰفِعُ لِلنَّاسِ ...

... And we sent down Iron, wherein is great strength and benefits for humankind ...

Surah Al-Hadid (Iron) 57:25

I gratefully acknowledge mentorship of Dr. Tracy W. Nelson and Dr. Carl D. Sorensen as well as support of my beloved parents, Mohammad-Reza Abbasi and Farah-Banou Azhdehakosh. The author would also like to thank Dr. B.L. Adams, Mr. J.A. Basinger, Dr. S. Ahmadi, and Dr. J. Farrer at Brigham Young University as well as Dr. S. Wright at EDAX-TSL for their helpful guidelines. This research was performed as part of the National Science Foundation’s Center for Friction Stir Processing: part of their Industry/University Cooperative Research Centers.

TABLE OF CONTENTS

LIST OF TABLES

LIST OF FIGURES

1 INTRODUCTION

This dissertation is composed of three chapters excluding the introduction and future work chapters. Each chapter addresses current issues in microstructural evolution study of Friction Stir Welded steels. They are presented as publishable journal papers.

Successful large scale prior austenite reconstructions have not been previously performed in order to recover pre-transformed microstructure and study microstructural evolution. The first chapter (paper) introduces an approach to reconstruct prior austenite grain structure and recover its orientation using Electron Backscattered Diffraction (EBSD) from room temperature microstructure. This approach is used for texture studies and variant selection analysis in subsequent chapters.

Lack of elevated temperature microstructural data has led to lack of understanding of deformation and phase transformation. In the second chapter, prior austenite microstructure was reconstructed. Reconstructed prior austenite texture as well as room temperature ferrite texture were studied in order to understand deformation and phase transformation behavior of friction stir welded high strength low alloy steels.

Variant selection in phase transformation of steels has been studied for many years. However, lack of large scale statistical microstructural data on prior austenite has led to non-conclusive theories and models. In the last chapter, variant selection in friction stir welded high strength low alloy steels is investigated using large scale prior austenite reconstructions. Results are presented and discussed.

2 AN APPROACH TO PRIOR AUSTENITE RECONSTRUCTION

2.1 Preface

One area of interest in Friction Stir Welding (FSW) of steels is to understand microstructural evolution during the process. Most of the deformation occurs in the austenite region. Quantitative microstructural measurements of prior austenite microstructure are needed in order to understand evolution of the microstructure. Considering the fact that room temperature microstructure in ferritic steels contains very little to no prior austenite, prior austenite microstructure needs to be recovered from the room temperature ferrite. In this paper, an approach based on Electron Backscattered Diffraction (EBSD) and phase transformation orientation relationships is introduced to reconstruct prior austenite grain structure and recover its orientation. This approach can be used to study microstructural evolution, phase transformations, and variant selection in materials that undergo allotropic phase transformations.

2.2 Introduction

Friction Stir Welding (FSW) is a hot deformation process. Most of the deformation occurs at elevated temperatures in steels and Ti alloys. It is well accepted that the peak temperature in FSW is about 0.6-0.95 melting point depending on the material, tool design and welding parameters [1]. Understanding microstructural evolution plays a key role in process optimization and property improvement.

Microstructural evolution has been studied extensively in single phase alloys (such as Al, Mg, and Cu). Hot deformation occurs in the same phase as the room temperature phase in these materials. Fast cooling after hot deformation has a quenching effect on the elevated temperature phase. Elevated temperature microstructure can be captured at room temperature. Information about elevated temperature texture and grain structure can thus be obtained via studying room temperature microstructure [2-5]. It is difficult to use the same approach to obtain elevated temperature information in alloys that undergo allotropic phase transformations.

The elevated temperature phase is consumed by the room temperature phase during the transformation in allotropic materials. The room temperature phase has a different crystal structure. The deformation history, texture, and grain structure of the elevated phase are altered or obscured by the phase transformations.

Recovering the grain structure and texture of the pre-transformed phase is crucial for understanding microstructural evolution in terms of hot deformation studies. Difficulty in reconstructing pre-transformed phases leads to a lack of hot deformation and microstructural evolution understanding in allotropic systems such as steels, titanium, cobalt, zirconium, uranium, and plutonium alloys.

Traditional approaches to recover elevated temperature microstructure in materials with allotropic phase transformation are inadequate. They can only recover very limited information about elevated temperature microstructure (prior austenite in the case of ferritic steels). Optical microscopy (OM) provides only morphological data such as prior austenite grain size. No crystallographic data can be obtained via OM. Its success heavily depends on segregation of alloying elements in prior austenite (PA) grain boundaries. It is partially successful on medium to high alloy steels [6].

Transmission Electron Microscopy (TEM) is very localized, tedious and time-consuming. It provides inadequate statistical data, and relies on retained austenite in order to obtain information about elevated temperature microstructure.

There have been several attempts to use Electron Backscattered (EBSD) data and phase transformation Orientation Relationships (OR's) to reconstruct prior austenite microstructure. Malet et. al. [7], He et. al. [8], and Furuhara et. al. [9] reconstructed several prior austenite grains using Kurdjumov-Sacks (KS) OR in order to study variant selection. Retained austenite was required in most of these reconstructions. Very little details on the reconstruction are available. Statistical data was limited due to limited number of reconstructed prior austenite grains. They proposed various variant selection mechanisms using the reconstruction results.

He et. al. [10-11] studied phase transformation in near-equilibrium cooled Iron meteorites. Ideal OR's such as KS and Nishiyama-Wasserman (NW) were investigated in order to determine which OR governs phase transformation under near-equilibrium conditions. A limited number of prior austenite grains were reconstructed with the help of retained austenite. No exact KS or NW OR's were observed.

Lambert-Perlade et. al [12] studied austenite to bainite transformation in the heat-affected zone of a high strength low alloy steel. They reconstructed several prior austenite grains using TEM and EBSD on retained austenite. The orientation relationship between austenite and bainite was reported to be close to KS and NW. As a result of this study, a two-stage phase transformation was proposed.

Cayron [13] has developed an automated process to reconstruct pre-transformed grain structure using EBSD. Pre-transformed phases in simple cases such as a bainitic steel with retained austenite, a martensitic steel, and two examples of Titanium alloys with both α and β phases present were reconstructed. A complex combination of symmetry and probability operators is used. Results demonstrated successful large-scale reconstructions. The methodology has been formalized into a commercial software package called ARPGE. However, the details regarding the approach are limited and the methodology is difficult to reproduce.

Preliminary results on the material of interest were unsatisfactory using ARPGE. Friction stir processed API X65 and HSLA-65 steel samples were analyzed. Prior austenite grains appeared very irregular and much larger than expected as compared to optical microscopy results.

Electron Backscattered Diffraction (EBSD) offers the advantage of large quantitative microstructural analysis. It provides large sets of statistical crystallographic and morphological data. It has the ability to obtain crystallographic data about room temperature phase. Well known phase transformation orientation relationships can be applied to the data to reconstruct elevated temperature phase orientation and texture. In order to better understand microstructural evolution, techniques need to be developed that can recover the elevated temperature microstructure.

The objective of this paper is to develop a method which can reconstruct PA grain structure and recover PA orientation. The intent is to achieve large scale reconstructions without relying on retained austenite.

2.3 Experiments

Bead-on-plate welds were performed on 9.5 mm thick API X80 plates. Poly crystalline Cubic Boron Nitride (PCBN) Convex-Scrolled-Shoulder-Step-Spiral (CS4) tool was used. The tool shoulder diameter and pin length were 36.8 mm and 4.5 mm, respectively. Chemical composition of the X80 plates was 0.04% C, 1.7% Mn, 0.135% Si, 0.41% Cr, and 0.537% (Ni+Mo+Al+V+Nb+Ti+N) in weight percent.

Position controlled welds were performed at tool rotational speed of 400 RPM and feed rate of 178 mm/min. Zero degree tilt was applied to the tool during welding. Argon gas was used as shielding gas to protect both the tool and the weld from surface oxidation. The welding direction was parallel to the plate rolling direction.

Water jet cutting was used to cut transverse metallographic samples. Samples were mounted in Bakelite then ground and polished successively through 1 μm diamond. Final fine polishing was done using 0.05 μm colloidal silica mixed with colloidal alumina at 10/1 ratio.

EBSD scans were performed on an FEI XL-30 SFEG scanning electron microscope equipped with TSL 5.2 OIM data collector/analyzer software. SEM accelerating voltage and spot size were 25 KV and 5, respectively. A hexagonal grid with the step size of 250 nm was used for the scans. The scan area was chosen in the advancing side of the weld. This area consists of a bainitic microstructure and has a higher hardness than the rest of the weld. Formation of this area is a topic of interest in FSW. Therefore, prior austenite reconstruction efforts were focused on this area.

2.4 Description of Reconstruction Methodology

There are well-established orientation relationships that relate ferrite to austenite. They express crystallographic relationships between these phases. Certain crystallographic planes and directions in ferrite are parallel to certain planes and directions in prior austenite. These relationships minimize the phase transformation strain energy by reducing the crystallographic mismatch between phases.

Kurdjumov-Sachs (KS) and Nishiyama-Wasserman (NW) are the two most widely accepted OR's in steels. KS and NW orientation relationships express the parallelism between austenite and ferrite by $\{111\}_\gamma//\{110\}_\alpha$ - $<110>_\gamma//<111>_\alpha$ and $\{111\}_\gamma//\{110\}_\alpha$ - $<112>_\gamma//<110>_\alpha$, respectively. However, it is recognized that there may not be an exact OR even in the case of near-equilibrium cooled iron meteorites [10, 11, 14]. KS and NW OR's result in 24 and 12 possible crystallographic orientations (variants) for ferrite from a given austenite orientation, respectively.

In this research, KS OR was used due to higher number of variants. Higher number of variants provides higher spatial resolution. KS variants are calculated and listed in Table 2-1.

Table 2-1. List of KS Variants

Variant #	**Austenite Plane**			**Austenite Direction**			**Ferrite Plane**			**Ferrite Direction**		
1	1	1	1	-1	0	1	0	1	1	-1	-1	1
2	1	1	1	-1	0	1	0	1	1	-1	1	-1
3	1	1	1	0	1	-1	0	1	1	-1	-1	1
4	1	1	1	0	1	-1	0	1	1	-1	1	-1
5	1	1	1	1	-1	0	0	1	1	-1	-1	1
6	1	1	1	1	-1	0	0	1	1	-1	1	-1
7	1	-1	1	1	0	-1	0	1	1	-1	-1	1
8	1	-1	1	1	0	-1	0	1	1	-1	1	-1
9	1	-1	1	-1	-1	0	0	1	1	-1	-1	1
10	1	-1	1	-1	-1	0	0	1	1	-1	1	-1
11	1	-1	1	0	1	1	0	1	1	-1	-1	1
12	1	-1	1	0	1	1	0	1	1	-1	1	-1
13	-1	1	1	0	-1	1	0	1	1	-1	-1	1
14	-1	1	1	0	-1	1	0	1	1	-1	1	-1
15	-1	1	1	0	-1	1	0	1	1	-1	-1	1
16	-1	1	1	-1	0	-1	0	1	1	-1	1	-1
17	-1	1	1	1	1	0	0	1	1	-1	-1	1
18	-1	1	1	1	1	0	0	1	1	-1	1	-1
19	1	1	-1	-1	1	0	0	1	1	-1	-1	0
20	1	1	-1	-1	1	0	0	1	1	-1	1	-1
21	1	1	-1	0	-1	-1	0	1	1	-1	-1	1
22	1	1	-1	0	-1	-1	0	1	1	-1	1	-1
23	1	1	-1	1	0	1	0	1	1	-1	-1	1
24	1	1	-1	1	0	1	0	1	1	-1	1	-1

KS OR produces a high degree of symmetry in pole figures. KS variants for a single austenite orientation are visually represented in <001> pole figures in Figure 2-1. Prior austenite and 24 ferrite <001> poles are marked by open diamonds and solid dots, respectively (Figure 2-

1a). Ferrite variants, which form three truncated squares, are centered around the prior austenite <001> poles. Each truncated square includes 8 of the 24 KS variants. There are two bars associated with each truncated square.

The combination of a truncated square and two related bars is called a Bain zone. There are total of three Bain zones as a result of complete transformation of austenite to 24 KS ferrite variants. The ideal pattern in Figure 2-1a is rotated off-axis to illustrate the geometry between Bain zones (Figure 2-1b). Ferrite variants in one Bain zone are marked in different numbers in Figure 2-1b showing one truncated square and its two associated bars.

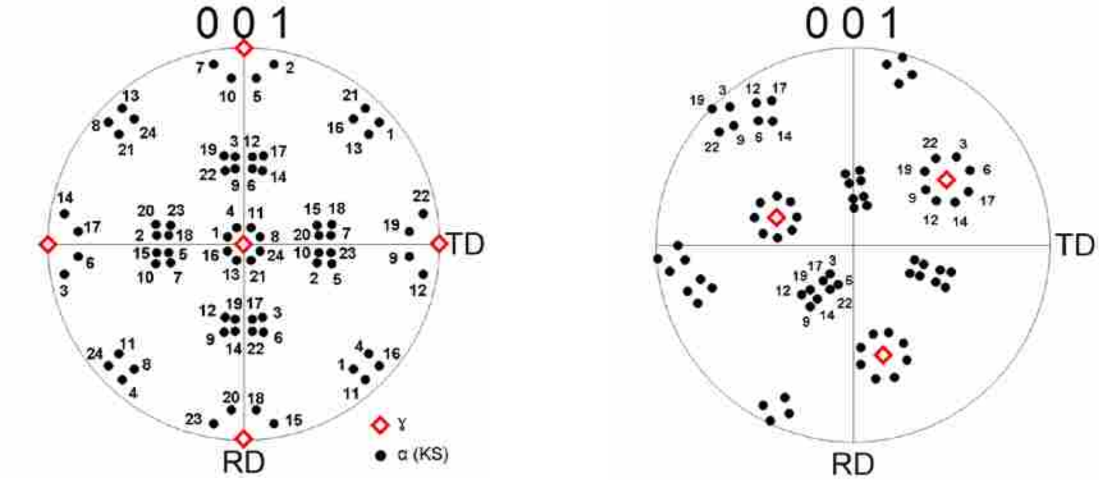

a b

Figure 2-1. Austenite <001>{100} pole figure showing KS variants (a), and <001> pole figure of a random austenite orientation highlighting KS variants in one Bain zone in different numbers (b). Prior austenite orientation is marked by red open diamonds in each pole figure.

Bain zones have a well-defined geometry relative to each other. Three truncated squares in the Bain zones are 90 degrees apart on connecting great circles (Figure 2-1b). This well-defined 90-degree geometry in <001> pole figures can be used to identify Bain zones that belong to the same prior austenite grain (PAG).

Rotating one Bain zone ±45 degrees about austenite <001> poles (center of its truncated square) overlays its bars onto the truncated squares of the other two Bain zones. This provides a quick check to see if Bain zones present in a <001> pole figure belong to the same prior austenite.

Prior austenite grain reconstruction involves a three step process. The first step is to identify and group the Bain zones that satisfy the ideal 90-degree geometry in <001> pole figures. The second is to assign associated ferrite grains from grouped Bain zones to one PAG. The last step is to iterate the process in order to reconstruct the whole PAG structure. Further details are explained in references [6, 15].

The reconstruction process of two prior austenite grains is shown in Figure 2-2. Figure 2-2a shows a grain map and <001> pole figure of two transformed prior austenite grains. Bainite packets belonging to different Bain zones in the left prior austenite grain are highlighted in blue, green, and red colors (Fig. 2-2b). These packets are all assigned to one PAG since their Bain zones satisfy the 90-degree geometry in ideal patterns (Fig. 2-2c). This PAG is colored in red in Fig. 2-2c. The rest of the packets are assigned to the neighboring prior austenite (blue grain in Fig. 2-2d). Blue Bain zones associating with these blue packets don’t match the geometry of the red Bain zones (red austenite grain). Blue Bain zones satisfy the ideal 90-degree geometry among themselves and all belong to the neighboring austenite grain (Fig. 2-2d).

One limitation of this pattern recognition technique is that it requires relatively well defined Bain zones (high number of active variants) in order to effectively reconstruct PAG. As the number of active variants increases, Bain zone detection becomes easier [6].

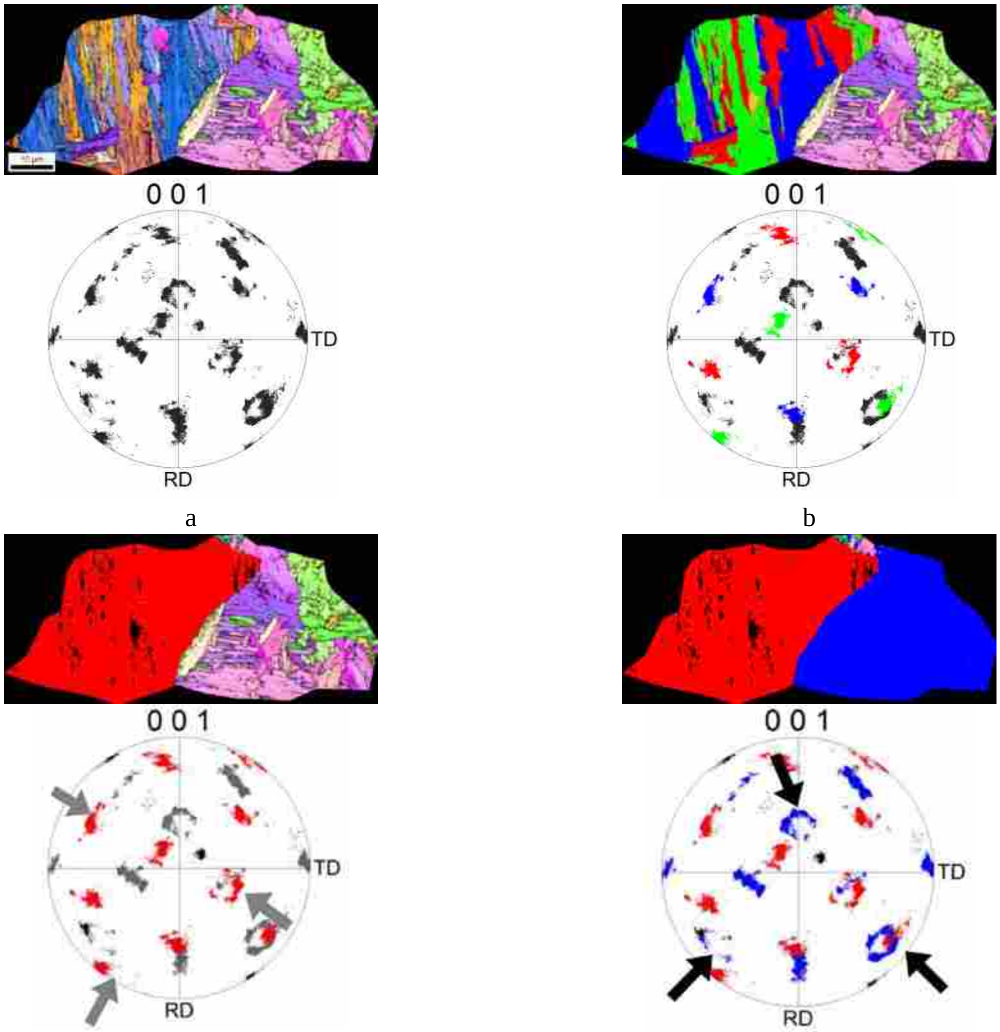

a b c d

Figure 2-2. The sequence of prior austenite grain reconstruction. a) Original cropped Inverse Pole Figure (IPF) map combined with Image Quality (IQ) map and its <001> pole figure. b) Highlighted bainite packets showing different Bain zones, c) Reconstructed prior austenite grain (red). d) Completed reconstruction of two PAG's. Truncated squares for both red and blue grains are indicated by arrows.

This prior austenite reconstruction technique is unable to recover the orientation of prior austenite. Centers of truncated squares in <001> pole figures are <001> poles of prior austenite (Fig. 2-1). However, 2-Dimensional projection of 3-Dimensional data in a pole figure distorts ideal spherical 90-degree geometry. Additionally, graphical methods require high number of active variants in order to identify centers of truncated squares. Errors due to EBSD and spread in data add to the difficulty of using graphical techniques to identify PA orientation. A separate approach is needed to find the crystallographic location of these centers which represent PA orientation. The approach will be discussed in detail.

Orientations are represented by Euler angles in Orientation Imaging Microscopy (OIM). Euler angles are three rotations that bring the sample coordinate system (RD, TD, ND) onto coincidence with a defined crystal coordinate system. Cube axes ([100], [010], [001]) are defined as crystal coordinate system in cubic systems. Euler rotations can be formulated into a matrix that represents the orientation dependence between two frames. This matrix is called coordinate transformation matrix; also known as g-matrix.

The coordinate transformation matrix (2-1) provides the overall rotation from sample coordinate system (S) to crystal coordinate system (C) [16]. Where, $g^{S \rightarrow C}$ is the coordinate transformation matrix or overall rotation (R) and (φ_1, Φ, φ_2) are three elements of Bunge's Euler angles. One of the properties of the g-matrix is that its inverse is equal to its transpose [16].

$$g_{ij}^{S \rightarrow C} = \begin{pmatrix} \cos\varphi_1 \cos\varphi_2 - \sin\varphi_1 \sin\varphi_2 \cos\phi & \sin\varphi_1 \cos\varphi_2 + \cos\varphi_1 \sin\varphi_2 \cos\phi & \sin\varphi_2 \sin\phi \\ -\cos\varphi_1 \sin\varphi_2 - \sin\varphi_1 \cos\varphi_2 \cos\phi & -\sin\varphi_1 \sin\varphi_2 + \cos\varphi_1 \cos\varphi_2 \cos\phi & \cos\varphi_2 \sin\phi \\ \sin\varphi_1 \sin\phi & -\cos\varphi_1 \sin\varphi & \cos\phi \end{pmatrix} \tag{2-1}$$

The orientation dependence between the sample coordinate system and the austenite coordinate system is unknown (R5 in Figure 2-3). Only ferrite orientations (in terms of Euler angles) are known (R1 in Figure 2-3). KS OR can be used to derive orientation dependence between ferrite and austenite coordinate systems. The approach to obtain austenite orientation (R5) is described below.

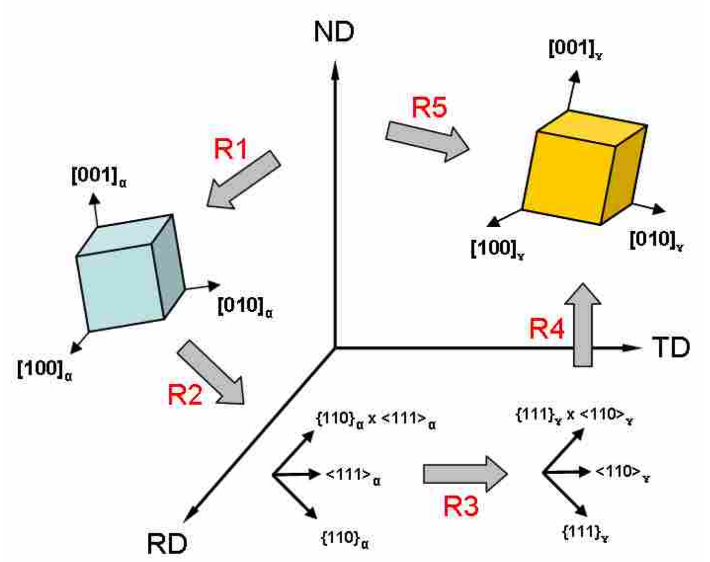

Figure 2-3. Schematic of rotations, sample frame (RD, TD, ND), ferrite cube frame, KS frame in ferrite, KS frame in austenite, and austenite cube frame

The ferrite to austenite phase transformation can be written as (2-2). It connects austenite to ferrite orientations for a fixed sample coordinate system.

$$\left(g_{ij}^{S\to\gamma}\right)=\left(g_{ik}^{\alpha\to\gamma}\right)\times\left(g_{kj}^{S\to\alpha}\right) \tag{2-2}$$

Where, S is the sample frame (RD, TD, ND), α is the cube frame ([100], [010], [001]) in the ferrite crystal, and γ is the cube frame ([100], [010], [001]) in the austenite crystal.

Solving (2-2) will provide possible prior austenite orientations. In order to solve (2-2), the term ($g^{\alpha\to\gamma}$) is required. This term is referred to as the Inverse Transformation Matrix.

Phase transformations are usually stated in the form of decreasing temperature (γ→α). Here, α→γ is defined as an inverse transformation. The relationship between inverse transformation matrices ($g^{\alpha\to\gamma}$) and transformation matrices ($g^{\gamma\to\alpha}$) is described by (2-3).

$$\left(g_{ik}^{\alpha\to\gamma}\right)=\left(g_{ki}^{\gamma\to\alpha}\right)^{-1}=\left(g_{ki}^{\gamma\to\alpha}\right)^{T} \tag{2-3}$$

Orientations in OIM are based on cube frames ([100], [010], [001]). The inverse transformation matrix is required to establish orientation relationship between ferrite and austenite cube frames. KS OR only states the relationship between close packed planes and directions in austenite and ferrite. It is essential to obtain orientation dependence between ($[100]_\alpha$, $[010]_\alpha$, $[001]_\alpha$) frame in ferrite and ($[100]_\gamma$, $[010]_\gamma$, $[001]_\gamma$) frame in austenite. A series of frames and rotations are needed in order to obtain inverse transformation matrix based on KS.

Rotations to calculate inverse transformation matrix are formulated into three rotations. They are schematically shown in Figure 2-3. R2 is an inter-crystalline rotation from cube frame to KS frame in ferrite. R3 is a rotation from KS frame in ferrite to KS frame in austenite. R3 coordinate transformation matrix will be an identity matrix due to KS OR. R4 is an inter-crystalline rotation from KS frame to cube frame in austenite

The inverse transformation matrix (R2+R3+R4) gives possible austenite orientations relative to ferrite cube frame. Details of matrix operations will be described.

In this approach, the phase transformation is considered purely a rotation problem. This approach neglects the change in lattice parameter due to the transformation.

KS frames are set up to calculate the inverse transformation matrix. These frames are based on parallel planes and directions in the α and γ crystals. They are defined as α' and γ', respectively. 24 α' and 24 γ' frames can be formed. This leads to 576 total combinations.

KS frames in ferrite and austenite are coincident. An example of α' and γ' frames for variant 1 in Table 2-1 is given in Table 2-2. Euler angles corresponding to frames in Table 2-2 are given in Table 2-3.

Table 2-2. KS Coordinate Systems in Ferrite and Austenite for Variant 1 in Table 2-1

α' coordinate system			**γ' coordinate system**		
α'_1	**α'_2**	**α'_3** $= \alpha'_1 \times \alpha'_2$	**γ'_1**	**γ'_2**	**γ'_3** $= \gamma'_1 \times \gamma'_2$
0 1 1	-1 -1 1	2 -1 1	1 1 1	-1 0 1	1 -2 1

Table 2-3. Euler Angles (in Radians) for Cube to KS Frames in Table 2-2

α to α'			**γ to γ'**		
φ_1	**Φ**	**φ_2**	**φ_1**	**Φ**	**φ_2**
1.107	1.150	0.886	0.464	1.150	0.685

Calculating the inverse transformation matrix is explained below. Inverse transformation matrix ($g^{\alpha\rightarrow\gamma}$) can be written as:

$$\left(g_{ik}^{\alpha\rightarrow\gamma}\right) = \left(g_{il}^{\gamma'\rightarrow\gamma}\right) \times \left(g_{lm}^{\alpha'\rightarrow\gamma'}\right) \times \left(g_{mk}^{\alpha\rightarrow\alpha'}\right) \tag{2-4}$$

or;

$$\left(g_{ik}^{\alpha\rightarrow\gamma}\right) = \left(g_{li}^{\gamma\rightarrow\gamma'}\right)^T \times \left(g_{lm}^{\alpha'\rightarrow\gamma'}\right) \times \left(g_{mk}^{\alpha\rightarrow\alpha'}\right) \tag{2-5}$$

Where, α' is <011>, <111>, <011>×<111>=<112> frame in the ferrite crystal and γ' is <111>, <011>, <111>×<011>=<112> frame in the austenite crystal.

Inter-crystalline transformation matrices ($g^{\alpha\text{-}\alpha'}$) or R2 and $(g^{\gamma\text{-}\gamma'})^T$ or R4 are required in order to calculate inverse transformation matrix ($g^{\alpha\text{-}\gamma}$) in (2-5). 24 coordinate transformation matrices from α to α' and 24 from γ to γ' can be calculated using KS frames in the form of Euler angles.

Additionally, intermediate coordinate transformation matrix ($g^{\alpha'\text{-}\gamma'}$) or R3 in (2-5) is equal to identity matrix (I). This is due to the KS OR and coincident α' and γ' frames.

Therefore, (2-5) simplifies to:

$$\left(g_{ik}^{\alpha\to\gamma}\right)=\left(g_{li}^{\gamma\to\gamma'}\right)^{T}\times\left(I\right)\times\left(g_{mk}^{\alpha\to\alpha'}\right) \tag{2-6}$$

Eventually;

$$\left(g_{ik}^{\alpha\to\gamma}\right)=\left(g_{li}^{\gamma\to\gamma'}\right)^{T}\times\left(g_{mk}^{\alpha\to\alpha'}\right) \tag{2-7}$$

Applying inter-crystalline transformation matrices to (2-7) gives 576 inverse transformation matrices. Cubic crystal symmetry reduces these 576 matrices to 24 matrices. Euler angles corresponding to these 24 inverse transformation matrices are listed in Table 2-4.

Table 2-4. List of Euler Angles (in Radians) for Inverse Transformation Matrices ($g^{\alpha\to\gamma}$)

Combination #	**φ_1**	**Φ**	**φ_2**	**Combination #**	**φ_1**	**Φ**	**φ_2**
1	1.993	0.181	3.564	**13**	3.564	0.181	1.993
2	6.172	0.735	0.250	**14**	1.459	0.735	4.962
3	4.824	0.735	1.321	**15**	0.112	0.735	6.034
4	2.719	0.181	4.290	**16**	4.290	0.181	2.719
5	3.391	0.735	3.030	**17**	4.962	0.735	1.459
6	1.321	0.735	4.824	**18**	2.892	0.735	3.253
7	3.253	0.735	2.892	**19**	4.463	0.735	1.682
8	1.149	0.181	5.861	**20**	0.250	0.735	6.172
9	1.820	0.735	4.601	**21**	5.861	0.181	1.149
10	6.034	0.735	0.112	**22**	1.682	0.735	4.463
11	0.422	0.181	5.135	**23**	3.030	0.735	3.391
12	4.601	0.735	1.820	**24**	5.135	0.181	0.422

Possible prior austenite orientations relative to the sample coordinate system (R5=R1+R2+R3+R4) can be generated by incorporating Table 2-4, into (2-7) and (2-2). Incorporating Euler angles from Table 2-4 into (2-7) forms 24 inverse transformation matrices. Applying these matrices to (2-2) for a given ferrite orientation generates 24 austenite coordinate transformation matrices. Euler angles for 24 possible prior austenite orientations can be calculated from these matrices using (2-1).

Each ferrite orientation generates 24 possible prior austenite orientations. At least two ferrite orientations are needed in order to recover PA orientation. Ferrite orientations originating from the same prior austenite grain should have at least two coinciding possible prior austenite orientations out of 24+24=48 total possible austenite orientations. Coinciding orientations are defined as possible prior austenite orientations that have low misorientations.

It requires 24×24= 576 misorientation comparisons to determine coinciding orientations. Averaging coinciding orientations will provide the orientation of prior austenite.

2.5 An Example

The present approach was applied to a prior austenite grain composed of several bainite packets in friction stir welded X80 steel (Figure 2-4a). There was no retained austenite to aid the identification of the austenite orientation. Absence of points at the centers of truncated squares in combined γ+α <001> pole figure (Figure 2-4b) implies that there is no retained austenite.

The sequence of finding coinciding orientations is shown in Figure 2-4. Four different orientations of ferrite from three different Bain zones were selected and highlighted (Orange, Purple, Green, and Red in Figure 2-4b). A tolerance angle of 2° was used. The orientations (Euler angles) for each of these ferrite were determined as (352, 82, 32), (181, 94, 54), (45, 30, 57), and (336, 30, 57), respectively.

24 possible orientations of prior austenite were calculated for each of the four ferrite orientations using relationships (2-1), (2-2), (2-7), and Table 2-4. These 24 possible prior austenite orientations for each ferrite are shown in <001> pole figures in Fig. 2-4c through 2-4f. They form three rings around ferrite <001> poles similar to the Bain zone patterns in Fig. 2-1.

Orientations with the lowest misorientations (coinciding orientations) were determined. These coinciding orientations for Orange, Purple, Green, and Red are (318.5, 108, 21), (222, 107, 70), (267.5, 27, 139), (88, 153, 311.5), respectively. Coinciding orientations are marked by arrows in Figures 2-4c through 2-4f. Misorientation between these points is less than 3.5 degrees (Fig. 2-4g).

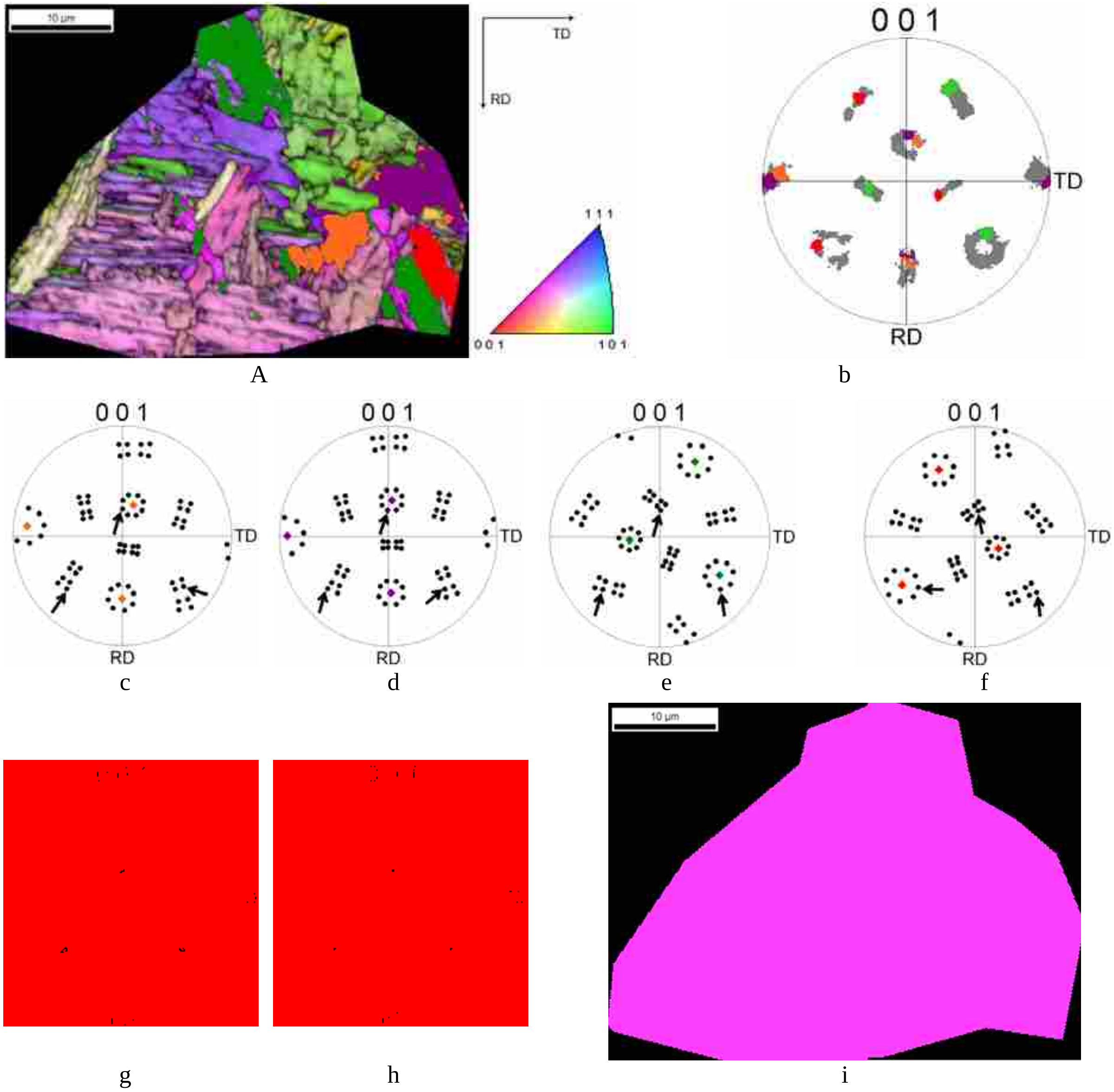

Figure 2-4. Sequence of prior austenite orientation recovery. a) Original cropped inverse pole figure + image quality map. b) Combined γ+α <001> pole figure highlighting 4 ferrite orientations. 24 possible prior austenite orientations for orange (c), purple (d), green (e), and red (f) ferrite, respectively. Ferrite orientations are marked by color diamonds. g) Coinciding prior austenite orientations before averaging. h) Prior austenite orientation (black) and its 24 ideal ferrite orientations in gray. Coinciding orientations are marked by arrows in each pole figure for orange, purple, green, and red ferrite. i) Inverse pole figure map of the reconstructed prior austenite.

Averaging coinciding orientations provides the orientation of prior austenite. Orientation of prior austenite is determined to be (270, 27, 45). Misorientation between prior austenite orientation and four coinciding orientations is less than 2 degrees. Recovered prior austenite orientation and its 24 ideal ferrite orientations are shown in Figure 2-4h. This matches the pole figure in Fig. 2-4b. The variants that attribute to the transformation of the recovered austenite to orange, purple, green, and red ferrite are V11, V4, V19, and V2 in Table 2-1, respectively.

Recovering prior austenite orientation is independent of which ferrite orientations are selected as long as they belong to the same austenite. They can be selected from any of the three Bain zones. Possible prior austenite orientations for different ferrite orientations should converge if they are transformed from the same prior austenite grain.

Inverse pole figure maps of ferrite and the reconstructed prior austenite are shown in Figure 2-5. Orientations from only 44 of the 68 reconstructed prior austenite grains in Figure 2-5b were recoverable. These grains were mostly medium to large size grains. Smaller grains had insufficient ferrite variants (one variant or two adjacent variants) to determine the coinciding prior austenite orientations. These grains are white in Fig. 2-5b. Orientation recovery becomes challenging or even impossible for small grains that have one or two adjacent variants.

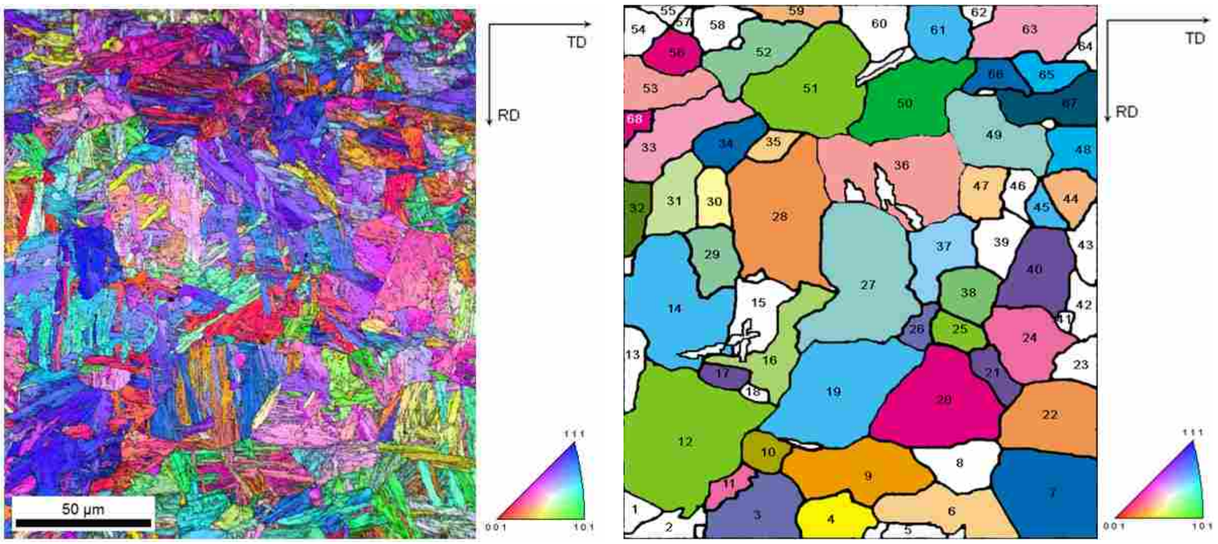

a

b

Figure 2-5. Inverse pole figure map combined with image quality map of the room temperature microstructure (a), and reconstructed prior austenite inverse pole figure map (b). Orientations of white prior austenite grains were not recoverable due to low number of active ferrite variants.

Most prior austenite grain boundaries are not identifiable in the room temperature microstructure (Figure 2-5a). This implies that ferrite grains along prior austenite boundaries have close crystallographic orientations (Figure 2-5a). Therefore, identifying prior austenite grain structure and orientation via ferrite-ferrite misorientation comparison will not provide satisfactory results. Austenite-ferrite misorientation comparison based on the current approach must be utilized in order to capture prior austenite boundaries and recover orientations.

It should be noted that the recovered orientation of prior austenite is relative to the orientations of ferrite. In the other hand, recovered prior austenite orientation may not necessarily represent true austenite orientation if ferrite orientations have changed due to heavy deformations after phase transformation.

2.6 Summary

Previous attempts on reconstruction have only been able to recover a few grains. Available software can only recover grain size and morphology of pre-transformed phases in some alloys. The current approach provides an effective tool to not only reconstruct large-scale grain structures, also to recover orientation of pre-transformed phase without relying on retained pre-transformed phase. This approach can be used to study phase transformation, variant selection, and to generate texture of elevated temperature phases to study hot deformation.

This approach has the potential to be incorporated into an automated software package as well as being performed manually. It can be generalized to other phase transformations in other materials as long as the phase transformation orientation relationship is known.

Higher number of active variants leads to more accurate reconstructions. At least two post-transformed variants are needed in order to recover orientation of pre-transformed phase.

3 TRANSFORMATION AND DEFORMATION TEXTURE STUDY IN FRICTION STIR PROCESSED API X80 STEEL

3.1 Preface

The nature of deformation in FSW is very complex. The degree of complexity increases even more when allotropic phase transformations are present. In this chapter, Electron Backscattered Diffraction (EBSD) is used as a means to reconstruct prior austenite (PA) texture and grain structure to study deformation and recrystallization in austenite and ferrite in FSW of HSLA steels. Analyses show evidence of shear deformation textures such as A1* (111)[-1-12], B (1-12)[110], and -B (-11-2)[-1-10], as well as rotated-cube (R) recrystallization texture in the reconstructed PA. Existence of rotated-cube texture as well as polygonal grain structure of PA implies that recrystallization is partially occurring in prior austenite. Room temperature ferrite exhibits well-defined shear deformation texture components. The observed shear deformation texture in the room temperature microstructure implies that FSW imposes deformation during and after the phase transformation. The evolution of both elevated and room temperature textures in FSW'ed API X80 steel are presented.

3.2 Introduction

Friction Stir Welding (FSW) has shown promising results as a solid-state joining process. Aluminum, Magnesium, Copper, and Titanium alloys are commercially being friction stir welded for various engineering applications [17-18]. Among these materials, Aluminum has been by far the most widely investigated, especially with regards to deformation and microstructural evolution [17-18].

Although there is growing interest in FSW of steels, much of the research to date has been feasibility studies [19-24]. Recently, there have been several investigations focused on developing correlations between process parameters and post-weld microstructure [25-26]. Wei has shown linear correlations between Heat Input and microstructural features such as bainite lath and packet size [26].

Despite these correlations, deformation and microstructural evolution in friction stir welded steels are not well understood. Understanding deformation and microstructural evolution facilitates microstructure-property-process parameter correlations. These correlations are essential in understanding and optimizing the process.

Investigating deformation in FSW of steels is challenging. Compounding the complexity of non-uniform material flow is the allotropic phase transformation present in steels. Phase transformations not only induce internal stresses, but they mask the thermal/mechanical history of the elevated temperature phase. The combination of these makes it difficult to characterize the deformation in FSW of steels.

Texture has been a useful tool for investigating deformation in FSW. Field et. al. and Sato et. al. have studied textures in FSW of aluminum alloys [27-28]. Shear components such as {110}<001> and {114}<221> were observed after rotating data to the appropriate coordinate system.

Nelson has observed {1-1-1}<110>, {-112}<110>, {001}<110> shear components and rotated-cube texture in friction stir welded 304 austenitic stainless steel [29]. Friction stir welded pure iron is reported to show a well-defined {11-2}<111> shear texture [30]. The fact that different FCC shear texture components are active in FSW'ed Al and 304 austenitic stainless steel may suggest that the deformation in FSW is process and material dependent.

Microstructures and weak shear textures observed in FCC alloys suggest that extended plasticity mechanisms such as dynamic recrystallization are active during the process [27, 29]. In steels and titanium alloys, both extended plasticity mechanisms and a phase change will affect the room temperature microstructure and properties.

In this research, both elevated and room temperature microstructures were studied to understand deformation and recrystallization in FSW'ed HSLA steels. Elevated temperature grain-structure and texture were reconstructed from room temperature microstructure using techniques explained in details in the previous chapter and reference [6]. Texture data in both elevated and room temperature phases were rotated to the appropriate shear coordinate system and compared to well known torsion test shear texture components in both FCC and BCC materials.

3.3 Experiments

Chemical composition of the X80 plate used in this study is shown in Table 3-1. Carbon equivalent (CE) and ferrite to austenite transformation temperatures (Ac1 and Ac3) were calculated as 0.43 weight percent, 713°C, and 800°C, respectively.

Table 3-1. Chemical Composition of X80 Steel Used in This Study

Element	C	Mn	P	S	Si	Cr	Cu	Ni+Mo+Al+V+Nb+Ti+N
Wt. %	0.04	1.7	0.013	0.001	0.135	0.41	0.263	0.537

Bead-on-plate welds were performed on 9.5 mm thick X80 plates. A Poly crystalline Cubic Boron Nitride (PCBN) Convex-Scrolled-Shoulder-Step-Spiral (CS4) tool was used. The tool shoulder diameter and pin length were 36.8 mm and 4.5 mm, respectively.

Position controlled welds were performed at a tool rotational speed of 400 RPM, and feed rate of 178 mm/min. Zero degree tilt was applied to the tool during welding. Argon gas was used as shielding gas to protect both the tool and the weld from surface oxidation. The welding direction was parallel to the plate rolling direction.

Water jet cutting was used to remove transverse metallographic samples. Samples were mounted in Bakelite then ground and polished successively through 1μm diamond. Final polishing was done using 50 nm colloidal silica mixed with colloidal alumina at 10/1 ratio.

Areas in the advancing side of the weld nugget were scanned using an FEI XL-30 SFEG scanning electron microscope (SEM) equipped with TSL 5.2 OIM data collector/analyzer software. SEM accelerating voltage and spot size were 25 KV and 5, respectively. Hexagonal grid with the step size of 250 nm was used for the EBSD scans.

EBSD data has to be rotated to the shear deformation coordinate system caused by rotation of the tool in order to study textures in FSW and compare them to known torsion textures. This rotation varies based on the tool geometry, location of EBSD scans, and sample configuration relative to the SEM coordinate frame. A schematic of FSW and the coordinate systems used in this study are shown in Figure 3-1.

Rotations were applied to EBSD data in order to observe textures in the local shear deformation frame. These rotations bring the electron microscope frame (RD, TD, ND) onto the local shear deformation frame (SD, SPN, XD). This way, shear direction (SD) and shear plane normal (SPN) of the scanned area coincide with rolling direction (RD) and transverse direction

(TD) of the microscope frame. This assists possible shear textures to reveal themselves in pole figures or Euler space sections.

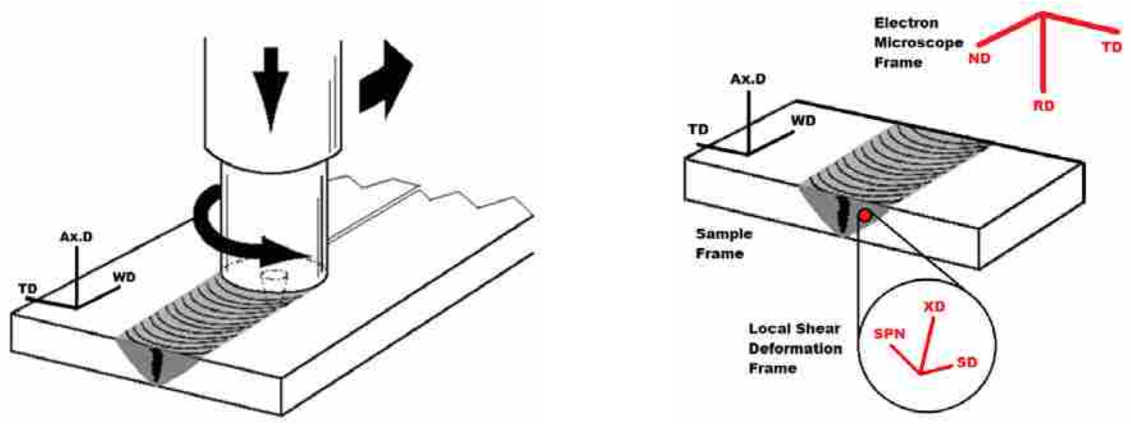

a b

Figure 3-1. Schematic of FSW (a) and schematic of sample used for EBSD analysis (b). Ax.D, WD, XD, SD, and SPN represent axial direction of the tool, welding direction, tool tangential direction, shear direction, and shear plane normal, respectively. Picture in (a) is a modified copy of picture in B. Nielsen MS thesis at Brigham Young University.

Based on the location of the scan and geometry of the tool (mainly tool probe half angle or θ=30°), the consecutive applied rotations (R1, R2, and R3) to EBSD data were estimated. These rotations were approximately R1= -90° about TD, R2 = -25° about RD, and R3= 170° about ND (see Fig. 3-1b and Fig. 3-2).

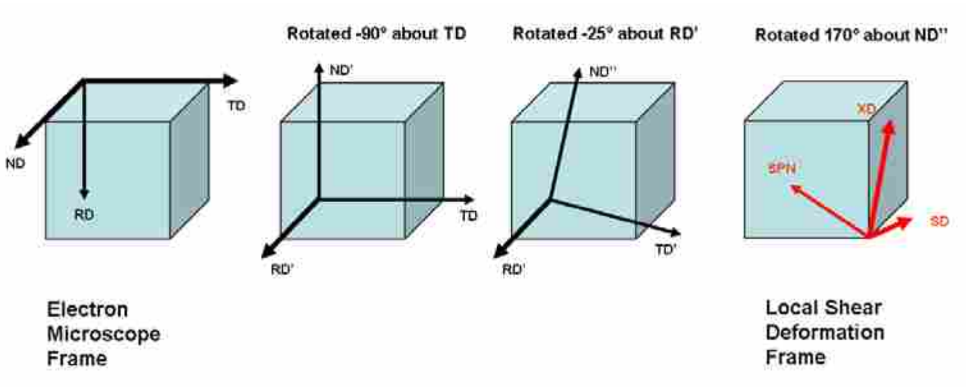

Figure 3-2. Schematic of applied rotations

Prior austenite grains were identified using <001> pole figure approach which is fully explained in chapter 2 and reference [6]. Orientation of each individual prior austenite grain (PAG) was determined from room temperature EBSD data utilizing Kurdjumov-Sachs (KS) transformation orientation relationships and matrix operations explained in chapter 2 in detail.

Each prior austenite orientation was then ideally transformed to ferrite using 24 KS variants. Texture of ideally transformed ferrite was generated and compared to the actual room temperature texture in order to investigate the effect of deformation and transformation on texture evolution.

3.4 Results and Discussion

Combined inverse pole figure/image quality map and the reconstructed prior austenite grain map are shown in Figure 3-3. Room temperature microstructure primarily consists of bainite (Figure 3-3a). The absence of original base metal polygonal ferritic microstructure in Figure 3-3a indicates that full austenitization has occurred during FSW at this parameter. This suggests that the temperatures in the weld nugget exceeded 800°C.

Reconstruction of the prior austenite phase shows a polygonal microstructure with the average grain size of 22 μm. Grains as large as 47 μm (grain 12) and as small as 6 μm (grain 57) can be seen (Fig. 3-3b).

Most prior austenite grain boundaries are not identifiable in the room temperature microstructure (compare Figures 3-3a and 3-3b). This implies that ferrite grains have close crystallographic orientations that make it difficult to identify prior austenite grains simply from a grain map.

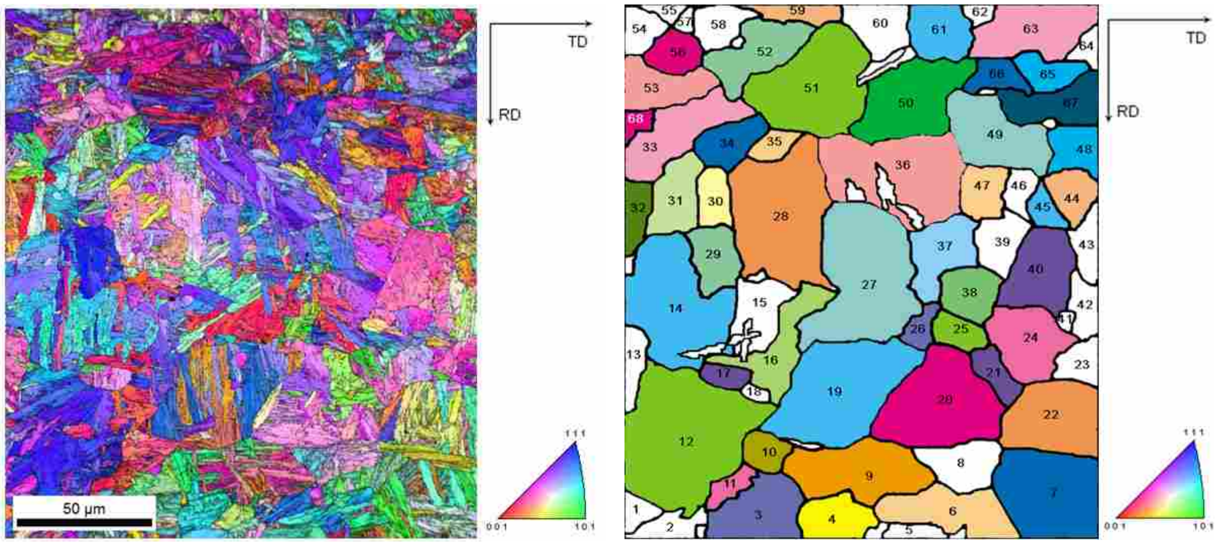

a

b

Figure 3-3. Inverse pole figure map combined with image quality map of the room temperature microstructure (a), and reconstructed prior austenite inverse pole figure map (b). Orientations of white prior austenite grains were not recoverable due to low number of active ferrite variants.

Orientations from only 44 of the 68 reconstructed prior austenite grains in Figure 3-3b were recoverable. These grains were mostly medium to large size grains. Smaller grains had insufficient variants to identify the Bain zones (white grains in Fig. 3-3b). This makes prior austenite orientation reconstruction very challenging or even impossible for small grains [6 and chapter 2].

Textures were generated for both the elevated temperature austenite phase and the room temperature ferrite phase. Additionally, an ideal ferrite texture was generated from the reconstructed PA. All 24 KS variants were used to generate the ideal ferrite texture.

There are two common methods to represent texture data: pole figures, which are a quick way of observing patterns, and Euler sections which offer more details. In pole figures, resolution is lost due to 3D to 2D data projection. However, Euler sections occupy larger space because of more details. In this paper, Euler section representations were used due to higher resolution. The main focus was on two sections $\varphi_2 = 0°$ and $\varphi_2 = 45°$ which have particular importance in steel processing [31].

Ideal torsion test shear components in FCC and BCC structures are shown in Figures 3-4a and 3-4b, respectively. Reconstructed prior austenite textures, ideal ferrite textures transformed from reconstructed PA, and actual room temperature ferrite textures are shown in Figures 3-4c, 3-4d, and 3-4e, respectively. These textures were compared to ideal FCC or BCC shear textures in order to identify the components. Fractions of shear components in austenite and ferrite were measured with 15° tolerance angle and shown in Figures 3-5a and 3-5b, respectively.

Evidence of FCC shear texture components in the reconstructed PA texture (Figure 3-4c) similar to those reported in torsion tests (Figure 3-4a) can be seen [31-33]. Components such as A1* (111)[-1-12], B (1-12)[110], -B (-11-2)[-1-10], and rotated-cube (R) {001}<1-10> are observed in austenite Euler sections (compare Fig. 4c and 5b). Some of these components have also been reported in friction stir welded 304 stainless steel [29].

There are additional peaks in the reconstructed prior austenite Euler sections that are not associated to known shear deformation components (Fig. 3-4b). However, these peaks do not appear to associate with recrystallization textures such as rotated-cube.

Among all present shear components in prior austenite, B is the most dominant observed component (Fig. 3-5a). Existence of other shear components such as –B and A1* implies that there are multiple shear components active at elevated temperatures. Multiple weak shear components in FSW have also been reported in other FCC materials such as Aluminum and 304 stainless steel [27-29].

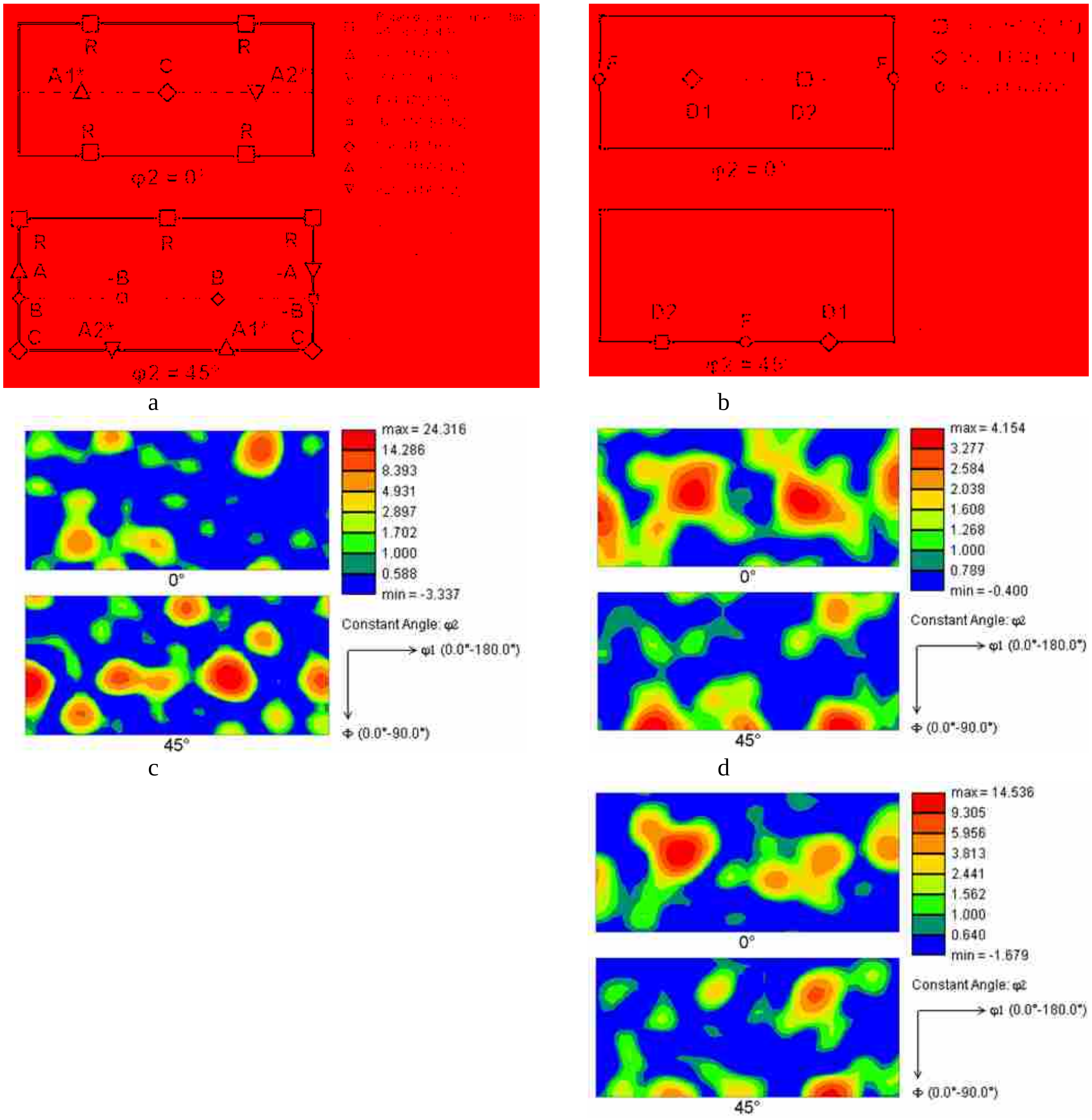

a b

c d

e

Figure 3-4. Euler space sections of: a) ideal FCC shear components, b) ideal BCC shear components, c) reconstructed prior austenite, d) ideally transformed ferrite (ideal ferrite) from reconstructed prior austenite, and e) actual room temperature ferrite.

The second highest fraction belongs to rotated-cube {001}<1-10> texture. Rotated-cube is a sign of dynamic recrystallization in FCC materials, especially in torsion test and mid-thickness hot rolling [29, 31, 33-35]. Continuous dynamic recrystallization due to continuous plastic deformation in FSW weakens shear textures. This is one possible reason why austenite does not exhibit strong deformation textures despite heavy shear deformation.

Evidence of weak BCC shear components such as D1 (-1-12)[111], D2 (11-2)[111], and F {110}<001> can be seen in ideal transformed ferrite (Fig. 3-4d). The maximum intensity of texture in ideal ferrite is low (4.154 times random). This suggests that the allotropic phase transformation contribution to the shear texture is insignificant.

Stronger D-component shear textures (both in terms of maximum intensity and area fraction) are observed in actual room temperature microstructure relative to ideal ferrite (Fig. 3-4d, Fig. 3-4e, and Fig. 3-5b). This is an indication of deformation occurring during and after the phase transformation.

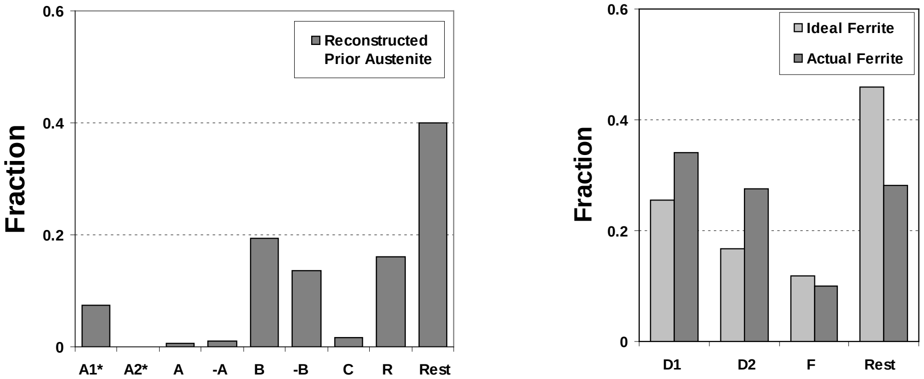

a b

Figure 3-5. Fraction of shear components in austenite (a) and ferrite (b)

A well-defined D-component shear texture was also reported by Mironov et. al. [30] in friction stir processed pure iron. The microstructure of the pure iron was primarily polygonal ferritic while that of the X80 steel is primarily Banitic. This suggests that FSW generates a distinctive D-component shear texture in BCC ferrite independent of cooling rate and ferrite morphology. Heavy deformations in ferrite can cause inaccurate prior austenite orientation recovery [chapter 3]. However in this case, deformation in ferrite was not heavy due to maintained Bain zone geometry in <001> pole figures in actual ferrite.

There are unidentified components in both ideal and actual ferrite (Figures 3-4d and 3-4e). They are mostly medium to low intensity peaks which are not associated with known BCC shear components. These may be results of the transformation of FCC shear components to BCC.

Ideal FCC shear components as well as rotated-cube component in Figure 3-4a were transformed to BCC using 24 KS variants in order to investigate the unidentified peaks. Texture plots of transformed FCC components are shown in Figure 3-6.

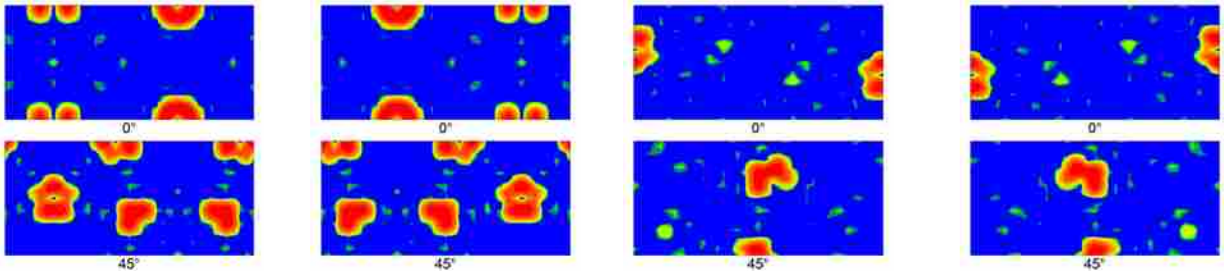

a) Transformed A1*
b) Transformed A2*
c) Transformed A
d) Transformed -A

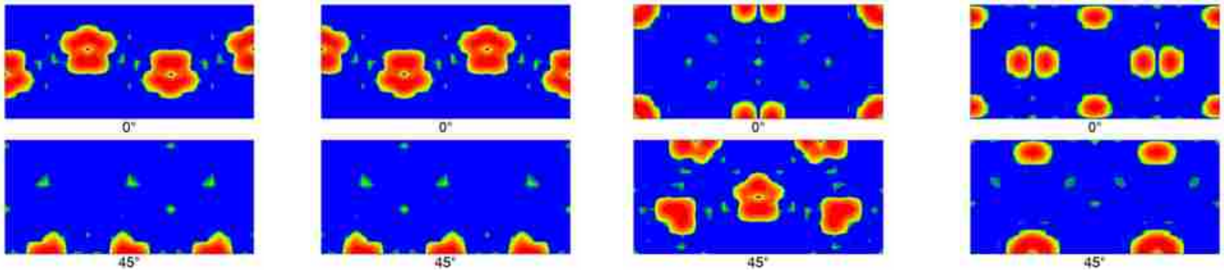

e) Transformed B
f) Transformed -B
g) Transformed C
h) Transformed Rotated Cube

Figure 3-6. Euler sections for ideally transformed FCC shear components to BCC

Transformed rotated-cube in ideal ferrite can be identified (compare Fig. 3-4d with Fig. 3-6h). This indicates that rotated-cube in austenite contributed to unknown peaks in ideal ferrite. However, no evidence of transformed rotated-cube in actual room temperature ferrite can be detected (compare Fig. 3-4e with Fig. 3-6h). This may suggest that mechanisms such as variant selection or deformation after phase transformation prevent formation of transformed rotated-cube in actual ferrite.

Combination of transformed B and -B appears similar to combination of D1, D2, and F components (compare Fig. 3-6e and 3-6f to Fig. 3-4c). However, peaks in the combination of transformed B and -B have very large spread relative to peaks in combined D1, D2 and F. Further investigations are needed to determine if ideal BCC shear components are related to ideal FCC shear components by transformation.

3.5 Summary

Evidence of A1* (111)[-1-12], B (1-12)[110], and -B (-11-2)[-1-10] shear textures in reconstructed prior austenite indicates that deformation is occurring at elevated temperatures. Fractions of these components were about 7%, 19%, and 13%, respectively.

Evidence of multiple weak textures and rotated-cube {001}<1-10> texture (with 16% fraction) in austenite as well as its polygonal grains suggest that recrystallization is partially occurring in austenite temperature range. This causes the shear texture in austenite to weaken.

Actual room temperature ferrite texture exhibits stronger D1 (-1-12)[111] and D2 (11-2)[111] shear texture components than ideal ferrite texture. This implies that deformation continues to occur after phase transformation. Deformation after phase transformation results in a stronger shear texture at room temperature.

4 VARIANT SELECTION MECHANISMS IN FRICTION STIR PROCESSED HIGH STRENGTH LOW ALLOY STEELS

4.1 Preface

Variant selection has been observed in HSLA steels. It has been studied in this research using techniques developed to reconstruct prior austenite grain structure and orientation. A hypothesis has been introduced based on interfacial energy and misorientation. Results support the hypothesis that variant selection is controlled by interfacial energy and misorientation. Variants that have near ideal FCC/BBC and near zero misorientations relative to their neighboring prior austenite and their neighboring ferrite, respectively, are selected to nucleate along prior austenite grain boundaries. This minimizes interfacial energy terms. Variant selection is mainly a grain boundary nucleation phenomenon. It occurs along prior austenite grain boundaries. Variant selection is more evident for small prior austenite grains. Intragranular area increases by increasing prior austenite grain size which increases intragranular nucleation of other variants. Results show no correlations between variant selection and maximum Schmid factor in prior austenite nor ferrite variants.

4.2 Introduction

Phase transformations are commonly observed in allotropic materials such as steels, Titanium, Cobalt, Zirconium, Uranium, and Plutonium alloys. Different phases with different crystal structures are stable under specific thermodynamic conditions (i.e. temperature and pressure). Parent phase transforms to daughter phase if thermodynamic conditions change.

Daughter phases consume the parent phase and introduce different crystal structures and orientations. A number of symmetrically equivalent daughter phase orientations result from the transformation of any given parent phase orientation. Each of these new orientations is called a variant. For instance, there are 24 BCC variants in Kurdjumov-Sacks (KS) Orientation Relationship (OR) for each FCC orientation.

Variant selection is an observed phenomenon that occurs in steel phase transformations. Theoretically, all variants have equal probability to occur. In reality, some variants are favored during phase transformations. This is called variant selection.

Post-transformed microstructure in steels is affected by variant selection. Fewer variants provide a coarser microstructure (polygonal ferrite). More variants induce higher local misorientations and lead to a finer microstructure (Martensite, Bainite, acicular ferrite, Widmanstatten ferrite).

Variant selection (VS) may affect post-transformed properties. Higher local misorientations and finer microstructures are favored in terms of resistance to crack propagation, strength, and ductility. High local misorientations may be detrimental in terms of magnetic and corrosion properties. Some variants may be favored in terms of microstructural design to provide optimum properties.

Understanding variant selection assists studying microstructural evolution. Microstructural evolution studies are needed to understand new processes such as Friction Stir Welding/Processing (FSW/P) and better understand Thermo-Mechanically Controlled Processing (TMCP). They facilitate parameter-microstructure-property correlations.

Several theories and models have been introduces on variant selection. They are mostly based on accommodating transformation strain or plastic deformation during phase transformation. These theories will be discussed briefly.

Variants that can accommodate Bain strain due to phase transformation are selected [12, 36]. FCC to BCC/BCT phase transformation induces dimensional changes which involve stretch and compression of the austenite unit cell. These dimensional changes are formulated as Bain strain model. Selection of these variants reduces the strain energy due to phase transformation. This model is commonly proposed in Martensitic transformations in steels.

In the presence of external elastic stress, interaction between Bain strain and applied stress is proposed as the mechanism for variant selection [36, 40]. Variants that can maximize the work done by stress are selected [36].

In some other theories, variants that have highest slip activity (high Schmid factors) are selected [38, 41]. This selection regime assists in accommodating plastic strains caused by the transformation when external or internal stresses exceed the flow stress.

M. Karlsen et. al. [42] studies variant selection in a room temperature austenitic-martensitic steel using EBSD and in-situ tensile testing. They concluded that variant selection in martensite is not controlled by slip system activity in austenite. As phase transformation progresses, no new martensite variants form or vanish, only the existing ones grow larger. They suggest that variant selection is a nucleation process.

L. Malet et. al. [7] studied variant selection in bainitic transformation of hot-rolled transformation-induced plasticity (TRIP) steels. They suggest packet selection instead of variant selection. A packet consists of variants with the same close-packed planes. They proposed that variant selection is based on the most active slip planes in austenite.

Y. He et. al. [8] studied crystallographic features of the γ-to-α transformation in a Nb-added TRIP steel using EBSD. They observed variant selection in un-deformed austenitic grains. No apparent variant selection in deformed austenite grains was detected. It was concluded that variant selection is not affected by plastic deformation.

N.J. Wittridge et. al. [43] studied austenite-martensite transformation in Fe-30%Ni after deformation by simple shear. They introduced a model based on the occurrence of in-plane reactions between glide dislocations for variant selection. Variants that have highest reactions between dislocations are selected and used for texture prediction.

T. Tomida et. al. [44] modeled variant selection to predict transformation texture in hot-rolled steels. In their model, variants nucleate in high angle prior austenite grain boundaries. Selected variants have near KS relation not only with their own grain, also with adjacent grains. They claimed that prediction of transformation textures in hot-rolled steels has become possible using the proposed model. However, there is very limited experimental data to validate their variant selection model.

T. Furuhara et. al. [9] studied variant selection in grain boundary nucleation of upper bainite in Fe-9Ni-0.15C steel. A two-stage variant selection mechanism is proposed. Bainitic ferrite that nearly holds KS orientation relationship with respect to austenite grain in which it grows is selected. Variants that can accommodate deformation strain become more active as transformation proceeds. Few prior austenite grain boundaries were investigated.

There are limitations to these models and theories. There is very limited experimental data to support above theories. These theories are mainly investigated on partially transformed steels. Both austenite and ferrite phases need to be present at room temperature in order to study relations between present variants and prior austenite grains. There is lack of statistical data on prior austenite. Very few prior austenite grains were studied due to inability to reconstruct prior austenite microstructure in large scales.

It is necessary to reconstruct prior austenite (PA) microstructure in ferritic steels in order to study variant selection. No to little residual austenite is available at room temperature microstructure in ferritic steels. Prior austenite microstructure is required. Recently, an approach was developed to reconstruct prior austenite grain structure and orientation [6 and chapter 2]. Variant selection can be investigated in large scales by having prior austenite and ferrite microstructures using this reconstruction approach.

The objective of this paper is to understand the fundamental mechanisms of variant selection in HSLA steels.

4.3 Experiments

Bead-on-plate welds were performed on 9.5 mm thick API X80 plates. Poly crystalline Cubic Boron Nitride (PCBN) Convex-Scrolled-Shoulder-Step-Spiral (CS4) tool was used. The tool shoulder diameter and pin length were 36.8 mm and 4.5 mm, respectively. Chemical composition of X80 plates was 0.04% C, 1.7% Mn, 0.135% Si, 0.41% Cr, and 0.537% (Ni+Mo+Al+V+Nb+Ti+N) in weight percent.

Position controlled FSW were performed at tool rotational speed of 400 RPM and feed rate of 178 mm/min. Zero degree tilt was applied to the tool during welding. Argon gas was used as shielding gas to protect both the tool and the weld from surface oxidation. The welding direction was parallel to the plate rolling direction.

Water jet cutting was used to cut transverse metallographic samples. Samples were mounted in Bakelite then ground and polished successively through 1 μm diamond. Final fine polishing was done using 0.05 μm colloidal silica mixed with colloidal alumina at 10/1 ratio.

Post-weld heat treatment was performed on selected FSW samples to achieve large prior austenite grains and study variant selection in large grain materials. Post-weld heat treatment releases stored strain energy caused by severe plastic deformation in FSW and often results in abnormal grain growth [45].

Samples for heat treatment were austenitized for 24 hours at 1200°C in an Argon controlled environment to obtain large austenite grains. They were immediately quenched and isothermally kept at a 450°C salt-bath for 3 hours to obtain Bainitic microstructure.

EBSD scans were performed on an FEI XL-30 SFEG scanning electron microscope equipped with TSL 5.2 OIM data collector/analyzer software. SEM accelerating voltage and spot size were 25 KV and 5, respectively. Hexagonal grid with the step size of 250 nm was used. Scanned area was chosen in the advancing side of the weld. The scan size for FSW and heat treated samples were 250×200 μm^2 and 800×400 μm^2, respectively.

Prior austenite grain structure and orientation were recovered from room temperature microstructure for both FSW and heat treated samples using techniques explained in chapter 2.

FSW can be modeled by torsion test since deformation is mainly shear. Orientation of grains in FSW must be brought to a local shear coordinate system in order to compare FSW data with torsion test data. Rotations are needed to bring FSW EBSD data into local shear deformation coordinate system [chapter 2].

Orientations of actual room temperature and reconstructed elevated temperature grains can be viewed in an orthogonal frame composed of Shear Plane Normal (SPN), Shear Direction

(SD), and Normal Direction (ND) after applying rotations. ND was selected as torsion axis. Details of these rotations are fully explained in chapter 2.

Maximum Schmid factors were calculated for 44 prior austenite grains in chapter 2. Schmid factors for ferrite orientations transformed from prior austenite grains were also calculated.

4.4 Preliminary Results and Discussion

Results show that not all variants are active during phase transformation. Three individual prior austenite grains and their <001> pole figures are shown in Figure 4-1. Not all Bain zones are complete in these grains. Detailed explanation of complete Bain zones is given in chapter 2. There are two active variants in one Bain zone in the first grain (Fig. 4-1a). About 6 active variants exist in one Bain zone in the second grain (Fig. 4-1b). About 18 variants are active in three Bain zones in the third grain (Fig. 4-1c).

Effect of Schmid factor in austenite and ferrite on variant selection for all 44 grains out of 68 prior austenite grains in chapter 3 was investigated. Prior austenite orientations for the rest of 68 grains were not recoverable. Results of Schmid factor analysis in austenite and ferrite variants are presented in following sections.

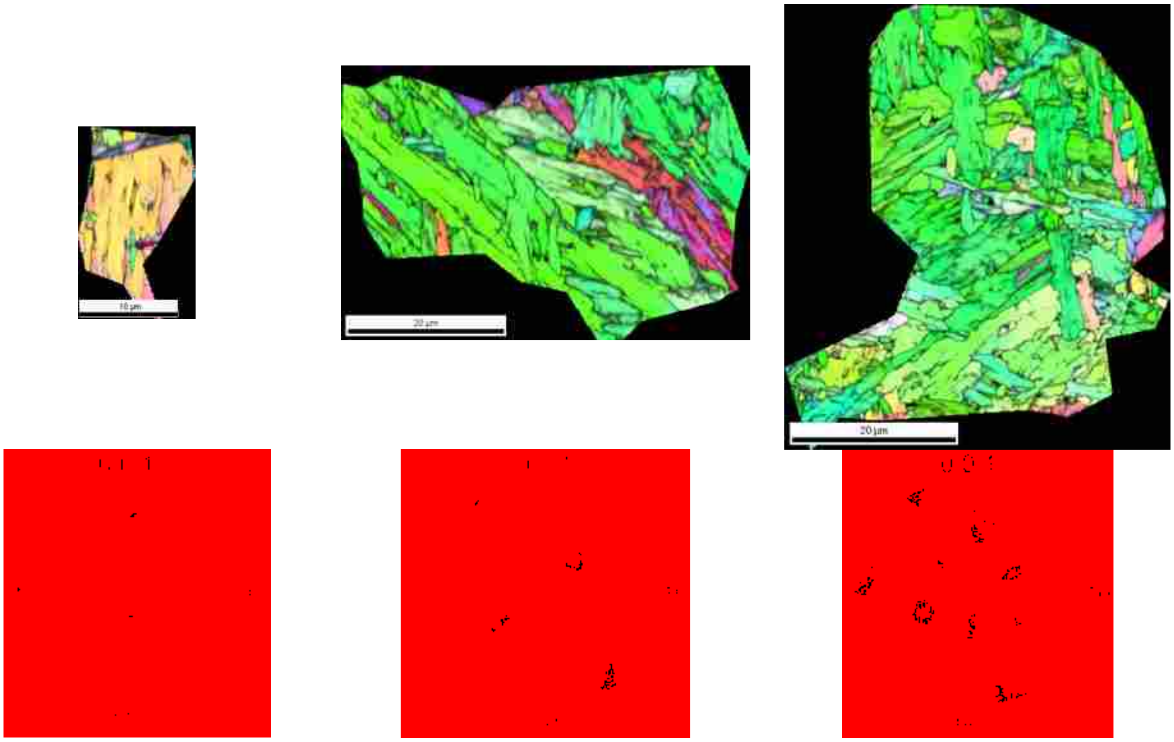

a b c

Figure 4-1. Inverse Pole Figure (IPF) combined with Image Quality (IQ) map of three prior austenite grains with different number of active variants in their <001> pole figures

There is no correlation between maximum Schmid factor in prior austenite and number of active ferrite variants (Figure 4-2). Higher Schmid factor in austenite does not limit the number of active ferrite variants. In other words, slip system activity in austenite does not govern variant selection in ferrite which is in agreement with Karlsen et. al. [42].

Possible correlations between maximum Schmid factor in ferrite variants and their presence were investigated. Data from three prior austenite grains ranging from 16-47 μm is presented. Prior austenite orientations for these three grains were recovered and ideally transformed to ferrite using approaches described in chapter 2. Maximum Schmid factors for ideal ferrite variants were calculated. Area fraction of each variant was measured by dividing the number of pixels within 2° misorientation of ideal ferrite variant orientation to the total number of pixels for that prior austenite grain.

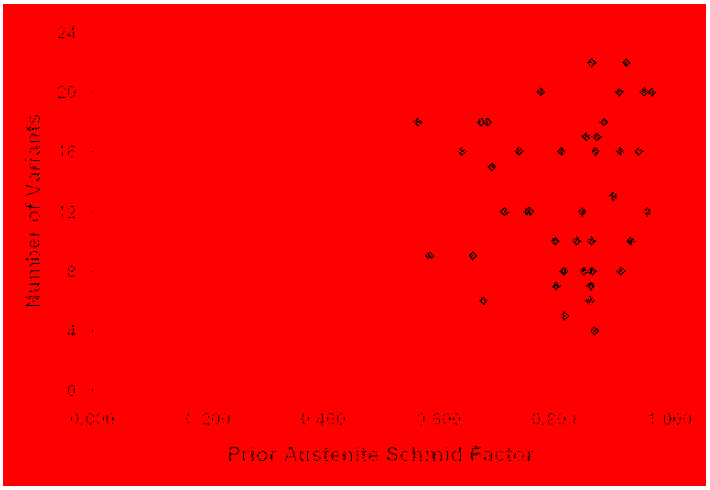

Figure 4-2. Number of active variants in austenite grains versus prior austenite maximum Schmid factor

Area fractions are plotted versus maximum Schmid factor in Figure 4-3. Inactive variants in these austenite grains have zero area fraction in the plots. There is no correlation between area fraction of active variants and maximum Schmid factor. Area fraction for some variants increases with increasing maximum Schmid factor (G #12 an G #22 in Fig. 4-3) while decreases for others (G #10 in Fig. 4-3c).

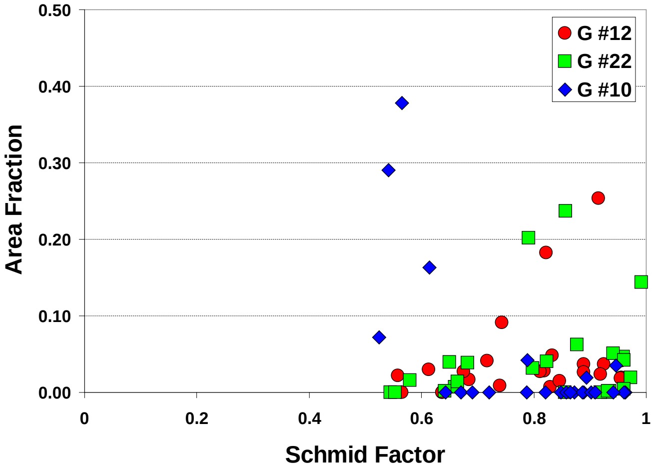

Figure 4-3. Area fraction of variants versus maximum Schmid factor of each variant for three prior austenite grains

Area fraction analysis shows that Schmid factor in ferrite does not govern variant selection contrary to references [38, 41]. Ferrite variants with the highest Schmid factors do not necessarily have the highest area fractions.

Preliminary results show no correlations between austenite (Fig. 4-2) or ferrite (Fig. 4-3) Schmid factor and variant selection. This implies that slip systems activity in austenite or ferrite does not govern variant selection.

Strong role of prior austenite grain size on the number of active ferrite variants was observed in FSW and heat treated samples. Larger prior austenite grains exhibit higher number of active variants (Figure 4-4). Analysis exhibits an increasing trend for number of active variants in prior austenite grains as prior austenite grain size increases. However, no strong variant selection was observed in the heat treated sample due to large PA grains. Average prior austenite grain size for the heat treated sample was 182 μm compared to 22 μm for FSW sample.

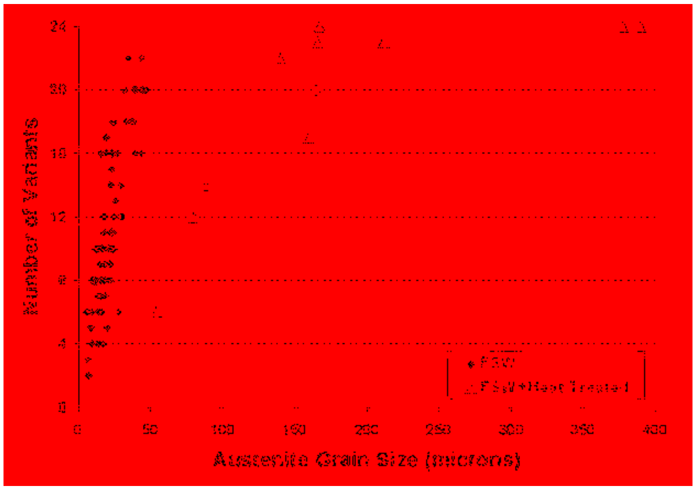

Figure 4-4. Number of active variants in austenite grains versus prior austenite grain size.

As prior austenite grain size increases, more boundary and intragranular areas become available in a given austenite grain. Therefore, more variants nucleate intragranularly in larger grains. However, the observed trend is unable to explain the cause for variant selection in grains of similar size. It only addresses prior austenite grain size effect. Different mechanisms must be involved in variant selection.

The authors propose that variant selection is driven by interfacial energy. Variant selection is assumed to be a nucleation process [42]. Ferrite variants that lead to the highest reduction in interfacial energy during ferrite nucleation would be selected. In order to investigate this hypothesis, classic heterogeneous nucleation theory is utilized.

Classic heterogeneous nucleation theory states that there are two competing terms in formation of a new nucleus. These energy terms are related to formation of new volumes and new interfaces. Change in free energy due to formation of a new volume is negative while formation of a new surface induces positive energy change.

Volume energy is highly dependent on temperature difference (undercooling). It can be assumed constant for a fixed temperature below the equilibrium transformation temperature. Interfacial energy has the most effects on change in free energy (ΔG) assuming a constant volume energy at a constant temperature.

Modified heterogeneous nucleation energy relationships for austenite to ferrite transformation are described in (4-1), (4-2), and (4-3). Two ferrite grains nucleate sequentially at the prior austenite grain boundary into their own prior austenite grains. They are shown schematically in Figure 4-5.

$$\Delta G_{I}^{Trans} = V_{\alpha_{1-i}} \Delta G^{V} + A_{\alpha_{1-i}-\gamma_1} E^{GB}_{\alpha_{1-i}-\gamma_1} + A_{\alpha_{1-i}-\gamma_2} E^{GB}_{\alpha_{1-i}-\gamma_2} - A_{\alpha_{1-i}-\gamma_2} E^{GB}_{\gamma_1-\gamma_2} \tag{4-1}$$

$$\Delta G_{II}^{Trans} = V_{\alpha_{2-j}} \Delta G^{V} + A_{\alpha_{2-j}-\gamma_2} E^{GB}_{\alpha_{2-j}-\gamma_2} + A_{\alpha_{2-j}-\alpha_{1-i}} E^{GB}_{\alpha_{2-j}-\alpha_{1-i}} - A_{\alpha_{2-j}-\alpha_{1-i}} E^{GB}_{\alpha_{1-i}-\gamma_2} \tag{4-2}$$

$$\Delta G_{Total}^{Trans} = \Delta G_{I}^{Trans} + \Delta G_{II}^{Trans} \tag{4-3}$$

γ_1 and γ_2 represent two adjacent prior austenite grains. $\alpha_{1\text{-}i}$ is the i-th ferrite variant transforming from γ_1 and nucleated from γ_1-γ_2 grain boundary, $\alpha_{2\text{-}j}$ is the j-th ferrite variant transforming from γ_2 and nucleated from γ_1-γ_2 grain boundary. ΔG^{Trans} is the change in free energy due to the phase transformation, and ΔG^{V} is the change in volume energy per unit volume due to the formation of a ferrite volume. E^{GB} is the interface energy per unit surface area (or grain boundary energy), V_α is the ferrite nucleus volume, and A is the interface area (grain boundary area).

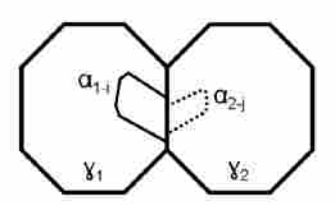

Figure 4-5. Schematic of ferrite nucleation from an austenite grain boundary

In this model, it is assumed that ferrite nucleates from prior austenite grain boundaries. This is a valid assumption since it has been experimentally shown that prior austenite grain boundaries are favorable sites for nucleation of structures such as grain boundary ferrite, Bainite, Martensite, and Widmanstatten ferrite [46-47].

It is also assumed that ferrite nucleation from prior austenite grain boundaries is sequential. Ferrite I ($\alpha_{1\text{-}i}$) in Figure 4-5 nucleates first and ferrite II ($\alpha_{2\text{-}j}$) nucleates after. Simultaneous nucleation of ferrite is still covered by the present model. There would be no $E_{\alpha_{1-i}-\gamma_2}^{GB}$ term in (4-1) and (4-2) in the case of simultaneous nucleation. Energy equations for ΔG_{Total}^{Trans} would be simplified to (4-4) assuming equal area for $\alpha_{1\text{-}i}$ and $\alpha_{2\text{-}j}$ at prior austenite boundary. The sequential model in (4-1) through (4-3) is chosen here because it includes all possible contributions to the free energy.

$$\begin{aligned}\Delta G_{Total}^{Trans} &= (V_{\alpha_{1-i}} + V_{\alpha_{2-j}})\Delta G^{V} + A_{\alpha_{1-i}-\gamma_1} E^{GB}_{\alpha_{1-i}-\gamma_1} + A_{\alpha_{2-j}-\gamma_2} E^{GB}_{\alpha_{2-j}-\gamma_2} \\ &+ A_{\alpha_{2-j}-\alpha_{1-i}} E^{GB}_{\alpha_{2-j}-\alpha_{1-i}} - A_{\alpha_{2-j}-\alpha_{1-i}} E^{GB}_{\gamma_1-\gamma_2}\end{aligned} \tag{4-4}$$

There are four types of interface boundaries in the present model (Figure 4-5 and relationships (4-1) through (4-3)). These boundaries are:

1- Interface between ferrite and the transforming austenite (($\alpha_{1\text{-}i}$-γ_1) in (4-1) and ($\alpha_{2\text{-}j}$-γ_2) in (4-2))

2- Interface between ferrite and the neighboring austenite ($\alpha_{1\text{-}i}$-γ_2) in (4-1)

3- Interface between two neighboring ferrite nuclei ($\alpha_{1\text{-}i}$-$\alpha_{2\text{-}j}$) in (4-2)

4- Interface between two neighboring austenite grains (γ_1- γ_2). Part of (γ_1-γ_2) interface is replaced by ($\alpha_{1\text{-}i}$-γ_2) interface

Effect of these interfaces on variant selection will be discussed in the following sections.

Interface between ferrite and the transforming austenite (($\alpha_{1\text{-}i}$-γ_1) in (4-1) and ($\alpha_{2\text{-}j}$-γ_2) in (4-2)) has no significant effect on variant selection. Near KS orientation relationship is met at these interfaces for all ferrite variants in order to reduce the mismatch. $E^{GB}_{\alpha_{1-i}-\gamma_1}$ or $E^{GB}_{\alpha_{2-j}-\gamma_2}$ are at their minimums. These energies are the same for all ferrite variants within their own austenite grains.

Interfacial energy between ferrite ($\alpha_{1\text{-}i}$) and the neighboring austenite (γ_2) varies from variant to variant. The lowest possible minimum value for $E^{GB}_{\alpha_{1-i}-\gamma_2}$ is equal to $E^{GB}_{\alpha_{1-i}-\gamma_1}$ when ferrite ($\alpha_{1\text{-}i}$) and the neighboring austenite (γ_2) meet near KS condition. This will provide the lowest mismatch.

Interfacial energy between ferrite ($\alpha_{1\text{-}i}$) and the neighboring ferrite ($\alpha_{2\text{-}j}$) varies from ferrite to ferrite. There are 24 possible ferrite for each austenite. Therefore, 24×24= 576 possible ferrite-ferrite combinations exist for two neighboring austenite grains. The lowest possible minimum value for ferrite-ferrite interfacial energy ($E^{GB}_{\alpha_{2-j}-\alpha_{1-i}}$) is zero when there is no boundary between ferrite ($\alpha_{1\text{-}i}$) and the neighboring ferrite ($\alpha_{2\text{-}j}$).

Prior austenite grain boundary energy ($E^{GB}_{\gamma_1-\gamma_2}$) for two given austenite grains (γ_1-γ_2) is constant. Selection of any ferrite variant in Fig. 4-5 does not change $E^{GB}_{\gamma_1-\gamma_2}$ since it is constant for two given austenite grains.

Among all four types of interfaces, ferrite ($\alpha_{1\text{-}i}$) and the neighboring austenite (γ_2) interface energy as well as ferrite ($\alpha_{1\text{-}i}$) and the neighboring ferrite ($\alpha_{2\text{-}j}$) interface energy are the only interfaces affected by variant selection. Low $E^{GB}_{\alpha_{1-i}-\gamma_2}$ can be achieved by selecting ferrite variants ($\alpha_{1\text{-}i}$) that have low mismatch with the neighboring austenite (γ_2). Low $E^{GB}_{\alpha_{2-j}-\alpha_{1-i}}$ can be achieved by selecting ferrite variants ($\alpha_{2\text{-}j}$) that have low mismatch with the neighboring ferrite ($\alpha_{1\text{-}i}$). This selection regime provides combination of variants in both austenite grains that minimize $E^{GB}_{\alpha_{1-i}-\gamma_2} + E^{GB}_{\alpha_{2-j}-\alpha_{1-i}}$.

$E^{GB}_{\alpha_{1-i}-\gamma_2}$ is controlled by misorientation between ferrite and the neighboring austenite. Grain boundary energy in general depends on large number of thermodynamic and geometric variables. Thermodynamic variables include temperature, pressure, and chemical potential of various components at the boundary [48]. They are assumed to be the same for all variants at $\alpha_{1\text{-}i}$-γ_2 boundary. Geometric variables are grain boundary misorientation and inclination [48].

Inclination of $\alpha_{1\text{-}i}$-γ_2 boundary is assumed to be the same for all ferrite variants along any given prior austenite grain boundary. Therefore, misorientation plays the most significant role in $E^{GB}_{\alpha_{1-i}-\gamma_2}$.

$E^{GB}_{\alpha_{2-j}-\alpha_{1-i}}$ is controlled by misorientation between ferrite ($\alpha_{1\text{-}i}$) and the neighboring ferrite ($\alpha_{2\text{-}j}$). Thermodynamic variables and inclination along the prior austenite boundary are assumed to be the same for all ($\alpha_{1\text{-}i}$-$\alpha_{2\text{-}j}$) combinations. Therefore, misorientation plays the most significant role in $E^{GB}_{\alpha_{2-j}-\alpha_{1-i}}$.

Misorientations that result in lower mismatch in $\alpha_{1\text{-}i}$-γ_1 and $\alpha_{1\text{-}i}$-$\alpha_{2\text{-}j}$ boundaries lower $E^{GB}_{\alpha_{1-i}-\gamma_2}$ and $E^{GB}_{\alpha_{2-j}-\alpha_{1-i}}$ the most. $\alpha_{1\text{-}i}$ variants with near KS misorientation relative to the neighboring austenite (γ_2) provide the lowest mismatch at the $\alpha_{1\text{-}i}$-γ_1 boundary. These variants are energetically favorable to nucleate in γ_1. $\alpha_{2\text{-}j}$ variants with the lowest misorientation relative to variants in γ_1 provide the lowest mismatch at the $\alpha_{1\text{-}i}$-$\alpha_{2\text{-}j}$ boundary. These variants are energetically favorable to nucleate in γ_2. The hypotheses can now be investigated by studying misorientations.

The minimum value for interfacial energies $E^{GB}_{\alpha_{1-i}-\gamma_2}$ and $E^{GB}_{\alpha_{2-j}-\alpha_{1-i}}$ can be achieved when $\alpha_{1\text{-}i}$ has near KS misorientation with γ_2 and near zero misorientation with $\alpha_{2\text{-}j}$, respectively. This provides the greatest negative value for total energy change (ΔG^{Trans}_{Total}) in (4-3). Austenite grain boundaries that exhibit these misorientation conditions will provide the largest driving force for variant selection.

In order to meet near KS condition between $\alpha_{1\text{-}i}$ and γ_2, {111} close-packed planes in γ_2 must be parallel to {110} close-packed planes in $\alpha_{1\text{-}i}$. This maintains continuity between close-packed planes in ferrite and the neighboring austenite.

Parallel close-packed planes between $\alpha_{1\text{-}i}$ and γ_2 can be achieved when γ_1-γ_2 has zero misorientation (no-boundary) or when it is a <111> twist boundary. Zero misorientation at γ_1-γ_2 (no-boundary) maintains parallelism between {111} close-packed planes in γ_1 and γ_2. It provides KS relationship at $\alpha_{1\text{-}i}$-γ_2 boundary and zero misorientation for $\alpha_{1\text{-}i}$-$\alpha_{2\text{-}j}$. It acts as a homogeneous nucleation site for ferrite in a larger austenite (γ_1+γ_2).

Austenite <111> twist boundary also puts {111} close-packed planes in γ_1 parallel to {111} close-packed planes in γ_2. This maintains continuity between {111} close-packed planes in γ_2 and {110} close-packed planes in $\alpha_{1\text{-}i}$. It meets planar condition of KS at the $\alpha_{1\text{-}i}$-γ_2 and $\alpha_{2\text{-}j}$-γ_1 boundaries.

Austenite tilt and non-<111> twist boundaries do not necessarily maintain parallelism between {110} close-packed planes in $\alpha_{1\text{-}i}$ and {111} close-packed planes in γ_2. These increase misorientation between close-packed planes and move away from near KS planar condition.

Austenite <111> twist boundaries were investigated further in order to determine the effect of austenite to austenite misorientation on variant selection.

Two austenite orientations were used to simulate transformation of austenite <111> twist boundaries. The first austenite orientation was chosen as <001>. The second austenite orientation was generated by rotating the first austenite θ degrees about <111>. The range and increments for θ were 0°-120° and 2.5°, respectively. Both <001> austenite and rotated austenite orientations at each θ were transformed to ferrite using 24 KS variants to investigate ferrite-ferrite misorientations [chapter 2].

Ferrite to ferrite ($\alpha_{1\text{-}i}$-$\alpha_{2\text{-}j}$) misorientation comparisons were performed for each austenite <111> twist boundary in order to determine minimum ferrite-ferrite misorientations. 576 ferrite-ferrite misorientations were compared for each austenite <111> twist boundary increment.

Minimum ferrite-ferrite ($\alpha_{1\text{-}i}$-$\alpha_{2\text{-}j}$) misorientation angles are plotted versus austenite <111> twist angle (θ) in Figure 4-6.

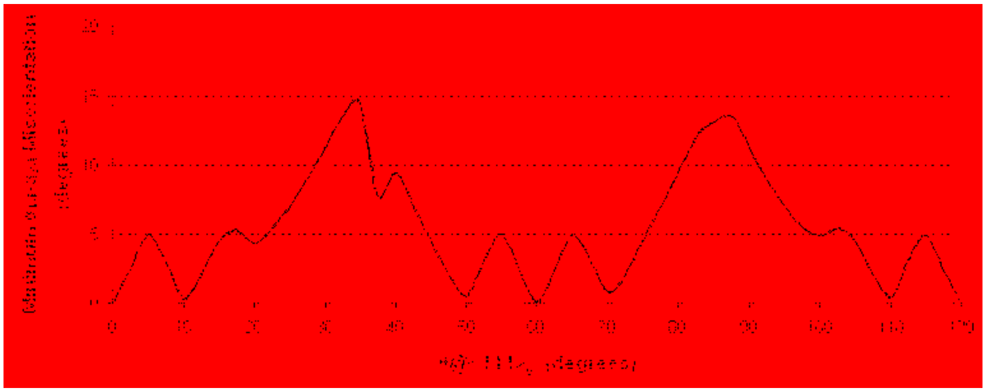

Figure 4-6. Minimum ferrite-ferrite ($\alpha_{1\text{-}i}$-$\alpha_{2\text{-}j}$) misorientation versus twist about <111> in austenite

Austenite <111> twist boundaries with 10°, 50°, 60°, 70°, and 110° degrees twist angle exhibit the lowest ferrite-ferrite misorientations. This excludes 0° and 120° twist angles which are no-boundary. 60°@<111> austenite twist boundary exhibits the lowest ferrite-ferrite misorientation among all <111> twist boundaries (Fig. 4-6).

Pole figures of transformed austenite 10°, 50°, 60°, 70°, and 110° twist boundaries are shown in Figure 4-7, respectively. Austenite 60°@<111> twist boundary is the only <111> twist boundary that exhibits coinciding variants (Fig. 4-6 and Fig. 4-7c). There are 12 coinciding variants out of 48 total variants in the 60°@<111> boundary (black dots in Fig. 4-7c). Misorientation between coinciding variants is about 0.1°. Minimum ferrite-ferrite misorientations for 10°, 50°, 60°, 70°, and 110° <111> twist boundaries are greater than 0.5° (Fig. 4-6). The number of variants contributing to the minimum misorientations for 10°/110° and 50°/70° <111> twist boundaries are 2 and 6, respectively (Fig. 4-7).

Coinciding variants in austenite 60°@<111> twist boundary satisfy near KS condition relative to their neighboring austenite. Misorientations between austenite and 24 ferrite variants transformed from the neighboring austenite in the 60°@<111> twist boundary are listed in Tables 4-1 and 4-2. 12 variants out of 48 total variants have near KS misorientation (variants 9, 12, 15, 18, 21, and 24 in Table 4-1 and Table 4-2). These were shown in Fig. 4-7c by black dots. Their misorientations relative to their neighboring austenite are 42.9°@<2 2 10.8> which deviate only about 0.2° from ideal KS (42.8°@<2 2 11>).

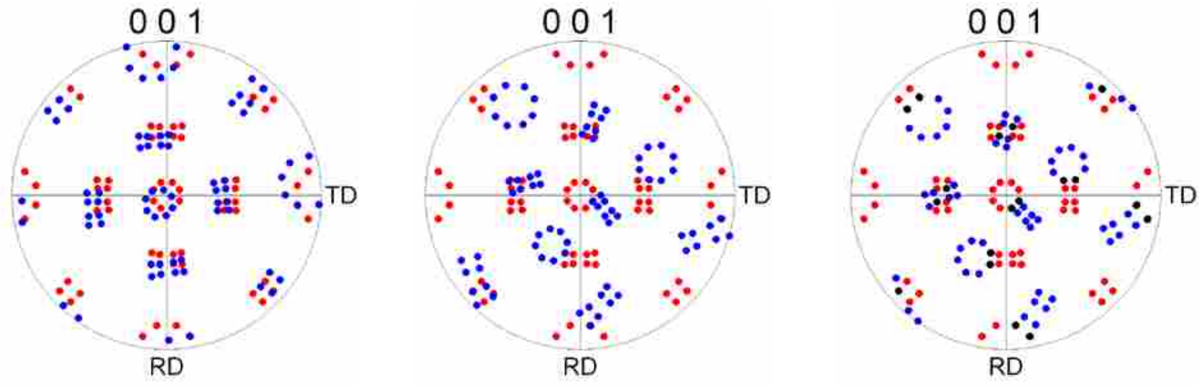

a) 10°@<111> b) 50°@<111> c) 60°@<111>

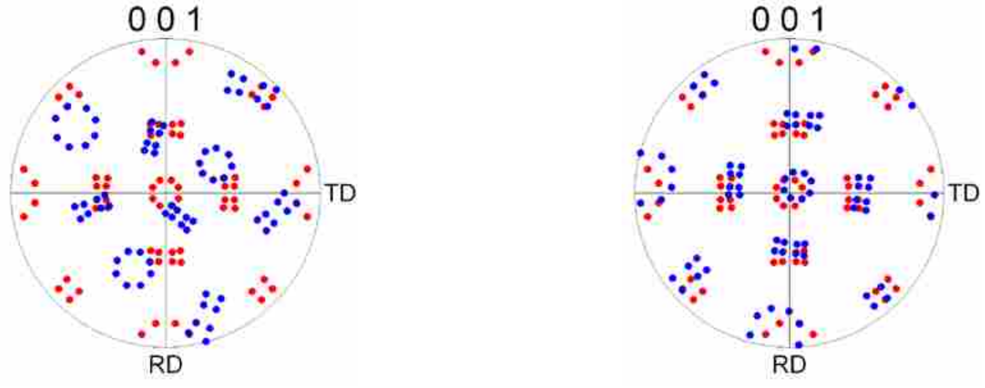

d) 70°@<111> e) 110°@<111>

Figure 4-7. <001> pole figures of austenite <111> twist boundaries that provide low ferrite-ferrite misorientations in Figure 4-6. Ferrite variants from <001> austenite and θ@<111> austenite are marked by red and blue dots, respectively. Coinciding variants in (c) are marked by black dots.

Coinciding variants meet the specific misorientations to minimize $E^{GB}_{\alpha_{2-j}-\alpha_{1-i}}$ and $E^{GB}_{\alpha_{1-i}-\gamma_2}$. This would produce the largest contribution to the overall phase transformation energy (ΔG^{Trans}_{Total}). As a result, these variants are energetically favored to nucleate along prior austenite grain boundaries.

Table 4-1. Misorientations in Terms of Rotation Angle and Axis Between Austenite with <001> Orientation and 24 Ferrite Variants Transformed From the Neighboring Austenite in 60°@<111> Configuration

Variant #	Rot. Angle	Rot. Axis [u v w]	Variant #	Rot. Angle	Rot. Axis [u v w]
1	49.5	-4 18 13	**13**	38.1	-2 16 7
2	49.5	4 -13 -18	**14**	38.1	-16 2 -7
3	49.5	18 13 -4	**15**	42.9	2 -2 10.8
4	49.5	-13 -18 4	**16**	42.9	-9 23 13
5	49.5	13 -4 18	**17**	42.9	-23 9 -13
6	49.5	-18 4 -13	**18**	42.9	2 -2 -10.8
7	38.1	7 -2 16	**19**	38.1	16 7 -2
8	38.1	-7 -16 2	**20**	38.1	2 -7 -16
9	42.9	10.8 2 -2	**21**	42.9	-2 10.8 2
10	42.9	13 -9 23	**22**	42.9	23 13 -9
11	42.9	-13 -23 9	**23**	42.9	9 -13 -23
12	42.9	-10.8 2 -2	**24**	42.9	-2 -10.8 2

Table 4-2. Misorientations Between Austenite with 60°@<111> Orientation and 24 Ferrite Variants Transformed from the Neighboring Austenite in <001> Configuration

Variant #	Rot. Angle	Rot. Axis [u v w]	Variant #	Rot. Angle	Rot. Axis [u v w]
1	49.5	-18 -13 4	**13**	38.1	-16 -7 2
2	49.5	-4 13 18	**14**	38.1	16 -2 7
3	49.5	-13 4 -18	**15**	42.9	2 2 -10.8
4	49.5	13 18 -4	**16**	42.9	13 -23 9
5	49.5	4 -18 -13	**17**	42.9	-13 -9 23
6	49.5	18 -4 13	**18**	42.9	-2 10.8 -2
7	38.1	2 -16 -7	**19**	38.1	-7 2 -16
8	38.1	7 16 -2	**20**	38.1	-2 7 16
9	42.9	-10.8 2 2	**21**	42.9	2 -10.8 2
10	42.9	9 13 -23	**22**	42.9	-23 9 13
11	42.9	23 -13 -9	**23**	42.9	-9 23 -13
12	42.9	-2 -2 10.8	**24**	42.9	10.8 -2 -2

4.5 Complimentary Results and Discussion

Active ferrite variants in prior austenite grain boundaries in both FSW and post-weld heat treated samples were studied. Two adjacent grains in FSW and two adjacent grains in post-weld heat treated samples are shown in Figures 4-8a and 4-8e, respectively. Corresponding Bain zones are highlighted in blue and red colors in <001> pole figures (Fig. 4-8b and 4-8f). Both pole figures meet the symmetry of transformed 60°@<111> boundary in Figure 4-7c. Measured misorientation between reconstructed prior austenite grains in both samples is near 60°@<111>.

Ferrite variants along prior austenite boundaries in Figures 4-8a and 4-8e are shown in Figures 4-8c, and 4-8g, respectively. Corresponding <001> pole figures for the variants along these grain boundaries are presented in Figures 4-8d and 4-8h, respectively. Ferrite variants present in these boundaries are highlighted in red and blue.

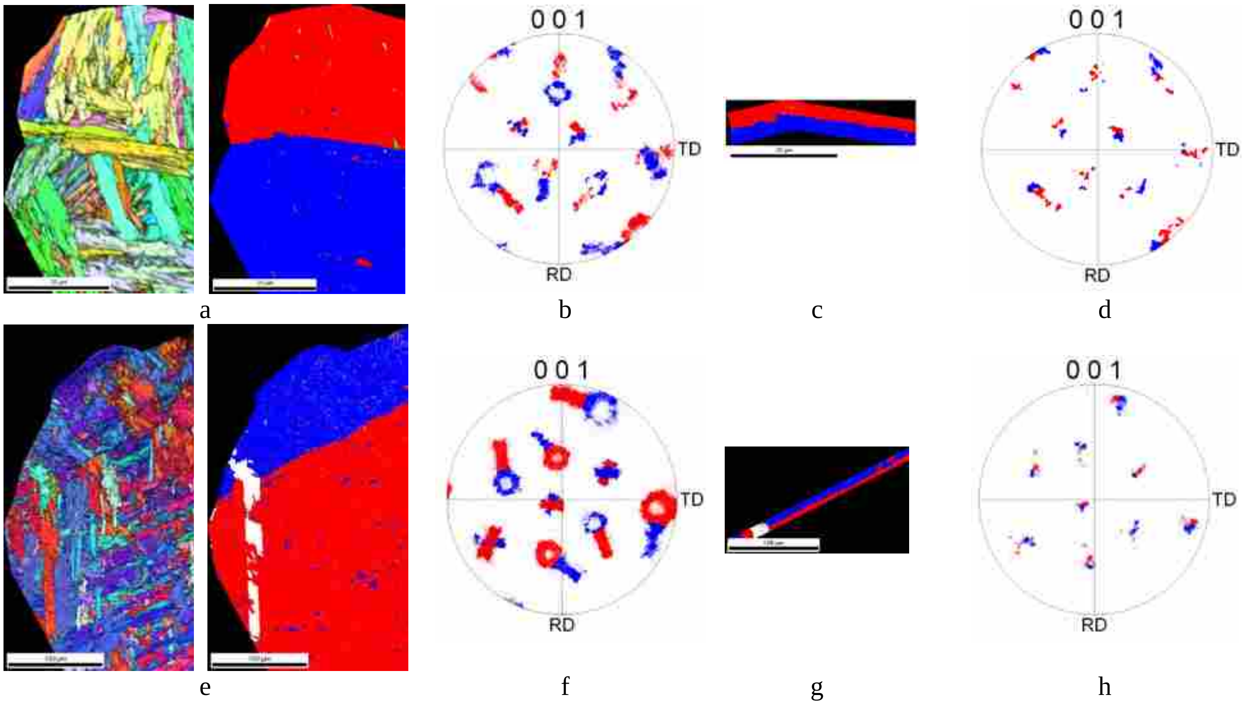

Figure 4-8. a) Inverse pole figure + Image Quality (IPF+IQ) and highlighted maps of two prior austenite grains in FSW sample. b) Their highlighted pole figure. c) Their cropped grain boundary showing active variants. d) Pole figure of active variants in the grain boundary. e) Inverse pole figure + Image Quality (IPF+IQ) and highlighted maps of two prior austenite grains in post-weld heat treated sample. f) Their highlighted pole figure. g) Their cropped grain boundary showing active variants. h) <001> pole figure of active variants in the grain boundary.

High fraction of ferrite variants along prior austenite grain boundaries have low ferrite-ferrite misorientation. This is evident by coinciding points in Fig. 4-8d and Fig. 4-8h. Low ferrite-ferrite misorientation minimizes $E^{GB}_{\alpha_{2-j}-\alpha_{1-i}}$. Additionally, these points have near KS misorientation relative to their neighboring prior austenite orientations which minimizes $E^{GB}_{\alpha_{1-i}-\gamma_2}$. Among these, 67% of blue variants and 73% of red variants present in the grain boundary of FSW sample in Fig. 4-8c lie within 42.8±5° of their neighboring austenite orientation, respectively. About 90% of active variants in the grain boundary of heat treated sample in Fig. 4-8g lie within 42.8±5° of their neighboring austenite orientation.

It should be noted that fewer variants in FSW sample are within the specified tolerance (42.8±5°) relative to their neighboring austenite orientation. However, it is shown that deformation occurs before, during, and after phase transformation in the FSW sample in chapter 3. Deformation during transformation would likely cause fewer variants to have near KS misorientation relative to their neighboring prior austenite. This will most likely happen for processes that deform the material in austenite-ferrite transformation region.

Further analysis of FSW and heat treated samples indicated that 40% and 65% of the total prior austenite boundaries were 60°@<111> twist boundaries, respectively. 5° tolerance angle was used for measurements. Given the fact that these boundaries make up large fractions of overall boundaries and coinciding variants are selected in them implies that austenite 60°@<111> boundaries have a large impact on variant selection.

Variant selection is mainly a grain boundary nucleation phenomenon. Coinciding variants provide near KS and near zero misorientations relative to their neighboring prior austenite and neighboring ferrite, respectively. This minimizes interfacial energy terms $E^{GB}_{\alpha_{2-j}-\alpha_{1-i}}$ and $E^{GB}_{\alpha_{1-i}-\gamma_2}$. Selection of coinciding variants along prior austenite 60°@<111> twist boundaries results in the greatest negative values for overall phase transformation energy (ΔG^{Trans}_{Total}).

Area fraction of non-coinciding variants increases by moving away from prior austenite 60°@<111> twist boundaries (Figure 4-9b). This confirms that variant selection is a grain boundary phenomenon and coinciding variants are selected at these boundaries. Increasing area fraction of non-coinciding variants by moving away from prior austenite boundaries suggests that variant selection is less significant inside large prior austenite grains due to intragranular nucleation of ferrite variants.

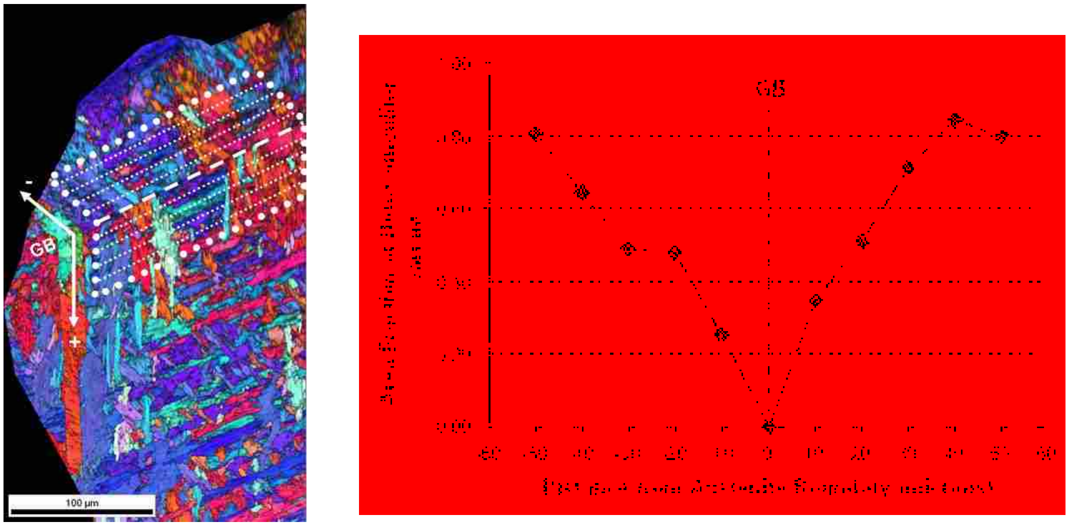

a b

Figure 4-9. Inverse pole figure + Image Quality map of two prior austenite grains in Figure 4-8e (a). 10-micron thick stripes are selected and marked in both sides of prior austenite grain boundary in order to avoid grain size effect on the number of active variants in each stripe. Area fraction of non-coinciding ferrite variants in each stripe were measured and plotted in (b).

Variant selection is more evident for small prior austenite grains. Lack of intragranular area in small prior austenite grains limits intragranular nucleation of other variants. Therefore, selected variants along the boundaries dominate small prior austenite grains.

As prior austenite grain size increases, the probability of intragranular ferrite nucleation increases. Intragranular ferrite nucleation can be either homogenous or heterogeneous (nucleation from particles or ferrite boundaries). Probability of intragranular nucleation is the same for all variants in the case of homogenous nucleation. Variants that are not selected at prior austenite grain boundaries nucleate intragranularly. This may explain the increasing trend for number of active variants versus prior austenite grain size observed in Fig. 4-4. Further investigations are needed to address intragranular nucleation and variant selection in large prior austenite grains. However, near complete Bain zones in Fig. 4-8b and Fig. 4-8f imply that variant selection is not significant in large prior austenite grains.

60°@<111> meets the misorientation of Σ3 coincidence site lattice (CSL) boundaries in FCC structures. Σ3 and other low-Σ boundaries in FCC structures are known to have low energies and especial properties [49-53]. Therefore, transformation in low-Σ austenite boundaries such as Σ5, Σ7, Σ9, and Σ11 was further investigated. None of these boundaries exhibited coinciding variants like Σ3 boundaries. The lowest ferrite-ferrite misorientations ($\alpha_{1\text{-}i}$-$\alpha_{2\text{-}j}$) achieved in transformed Σ5, Σ7, Σ9, and Σ11 boundaries were about 18°, 8°, 10°, and 1°, respectively. Selection of allotriomorphic ferrite variants that have near KS misorientation relative to neighboring austenite grains is also reported along austenite Σ11 boundaries by Kim et. al. [54] in a Fe-0.59C-0.98Si-1.1Mn-1.5Al wt%. steel.

It should be mentioned that Σ3 type boundaries cause difficulties in prior austenite reconstruction [6 and chapter 2]. Selection of coinciding variants at prior austenite Σ3 boundaries results in low ferrite-ferrite misorientations. Low ferrite-ferrite misorientation can cause inaccurate detection of exact prior austenite boundaries. It can result in larger PA grain sizes, irregular grain shapes, and inaccurate orientation recovery. Low Image Quality (IQ) values in EBSD assist detecting the exact prior austenite grain boundaries.

Further investigations of austenite Σ3 boundaries and their effect on room temperature microstructure and properties will be discussed in future papers.

4.6 Conclusions

Based on results and discussion, following conclusions can be made:

1- Variant selection is predominantly governed by grain boundary nucleation of ferrite along prior austenite boundaries. It is driven by misorientation. Variants are selected at prior austenite grain boundaries that have near Kurdjumov-Sacks (KS) misorientations relative to their neighboring prior austenite and near zero misorientations relative to neighboring ferrite grains.

2- Specific austenite boundaries such as 60°@<111> twist (Σ3) boundaries have strong impact of variant selection. Transformed prior austenite 60°@<111> twist (Σ3) boundaries provide near KS condition between ferrite and its neighboring austenite which minimizes ferrite-neighboring austenite interfacial energy. This results in near zero ferrite-ferrite misorientations which minimize ferrite-neighboring ferrite interfacial energies. There are 12 coinciding variants out of 48 total variants in transformed austenite 60°@<111> twist boundaries. Coinciding variants are selected to nucleate in these boundaries.

3- Prior austenite 60°@<111> twist (Σ3) boundaries compose a significant fraction of the elevated temperature microstructure. 40% of the elevated temperature grain boundaries in the friction stir welded sample are 60°@<111> twist (Σ3) boundaries. Fraction of these boundaries increases to 65% by post-weld heat treatment of the friction stir welded sample.

4- Number of active variants increases with increasing prior austenite grain size. Larger prior austenite grains have longer grain boundaries and more intragranular area available for more variants to nucleate and grow. Variants that have near KS and near zero misorientation with neighboring austenite and neighboring ferrite are selected along prior austenite grain boundaries. Other variants nucleate intragranularly as transformation progresses.

5- Variant selection becomes more significant as prior austenite grain size decreases. Variants intragranular nucleation decreases as prior austenite grain size decreases. Therefore, variant selection along grain boundaries becomes predominant for smaller prior austenite grains.

5 FUTURE WORK

Based on the findings of this research, following future investigations can be proposed.

1- Automating the reconstruction process. This enables reconstruction of the pre-transformed phase in shorter times. Large statistical data can be obtained utilizing the automated reconstruction tool in order to study microstructural evolutions in allotropic materials.

2- Investigating variant selection in austenite grain boundaries with random austenite-austenite misorientations. Variants that satisfy near KS and zero misorientations relative to their neighboring prior austenite and neighboring ferrite are selected in near <111> twist austenite boundaries. A design of experiments is required to generate austenite boundaries with random austenite-austenite misorientations in order to investigate if the same variant selection regime occurs.

One challenge is that random austenite-austenite misorientations do not necessarily provide high ferrite-ferrite misorientations and high deviations from KS. Minimum misorientations between ferrite variants do not reach high values (higher than 30°) due to the geometry of patterns containing six Bain zones transformed from two austenite grains. Therefore, high deviations from near KS condition would be difficult to achieve in order to study variant selection in austenite boundaries with random misorientations.

3- Investigating the effects of Σ3 boundaries in austenite on room temperature microstructure, mechanical, corrosion, and magnetic properties. Selection of coinciding variants in transformed Σ3 boundaries results in low ferrite-ferrite misorientations in prior austenite boundaries which can affect room temperature microstructure and properties.

4- Investigating relationships between nucleation and growth of grain boundary/polygonal ferrite and austenite Σ3 boundaries. It is reported that grain boundary ferrite maintains near KS relationship to one austenite grain and a random misorientation relative to the neighboring austenite. It is also reported that grain boundary ferrite grows into the austenite which has random misorientation. Austenite Σ3 boundaries may offer higher growth rates for grain boundary ferrite due to selection of coinciding variants. These variant can grow freely into both grains because they satisfies near KS with both grains.

5- Determining if variant selection has a significant impact on room temperature properties. Properties obtained in FSW and TMCP can be optimized by altering prior austenite grain size and controlling variant selection if it has an impact on properties. Results showed that larger prior austenite grains lead to higher number of variants and higher local misorientations. However, larger prior austenite grains may deteriorate mechanical properties such as fracture toughness and ductile to brittle transition temperature. Studies are needed to determine optimum prior austenite grain sizes.

6- Determining the contribution of FCC, BCC, and transformed FCC shear texture components on room temperature properties. For example, D1 and D2 shear components in BCC are frequently observed in FSW of steels and may be correlated to room temperature properties such as fracture toughness.

7- Determining if transformed FCC shear texture components are related to ideal BCC shear components. It was previously shown that the combination of transformed B and -B appears similar to the combination of D1, D2, and F components. Hot and cold torsion test simulations are needed in order to generate actual FCC and BCC shear components. Ideally transforming actual FCC components to BCC and comparing them to actual BCC components can reveal possible relationships between FCC and BCC components through phase transformation.

REFERENCES

1- T.R. McNelley, S. Swaminathan, J.Q. Su, Recrystallization Mechanisms During Friction Stir Welding/Processing on Aluminum Alloys, Scripta Mat. 58 (2008) 349-354

2- D.P. Field, T.W. Nelson, Y. Hovanski, K.V. Jata, Heterogeneity of Crystallographic Texture in Friction Stir Welds of Aluminum, Met. and Mat. Trans. 32A (2001) 2869-2877

3- Y.S. Sato, H. Kokawa, K. Ikeda, M. Enomoto, S. Jogan, and T. Hashimoto, Microtexture in the Friction-Stir Weld of an Aluminum Alloy, Met. and Mat. Trans; 32 A (2001) 941-948

4- M. Abbasi Gharacheh, et al., The influence of the ratio of ‘‘rotational speed/traverse speed (ω/v) on mechanical properties of AZ31 friction stir welds, Intl. J. Mach. Tools & Manuf. 46 (2006) 1983–1987

5- M. Amirizad, A.H. Kokabi, M. Abbasi Gharacheh, R. Sarrafi, B. Shalchi, M. Azizieh, Evaluation of microstructure and mechanical properties in friction stir welded A356+15% SiCp cast composite, Mat. Let. 40 (2006) 565–568

6- M. Abbasi, L.Y. Wei, T.W. Nelson, Prior Austenite Reconstruction in Friction Stir Processed API X65 Steel Using OIM, MS&T09, Oct. 2009, Pittsburgh, PA

7- L. Malet, M.R. Barnett, P.J. Jacques, S. Godet, Variant Selection during the Gamma-to-Alpha Phase Transformation in Hot-Rolled Bainitic Steel, Scripta Mat. 61 (2009) 520-523

8- Y. He, S. Godet, P.J. Jacques, and J.J. Jonas, Variant Selection During the γ-to-αb Phase Transformation in Hot-Rolled Bainitic TRIP-Aided Steels, Met. and Mat Trans. A 37A, Sept. 2006, p. 2641

9- T. Furuhara, H. Kawata, S. Morito, G. Miamoto, and T. Maki, Variant Selection in Grain Boundary Nucleation of Upper Bainite, Met. And Mat. Trans. A, 39 A, May 2008, 1003-1013

10- Y. He, S. Godet, J.J. Jonas, Representation of Misorientations in Rodrigues-Frank Space-Application to the Bain, K-S, N-W, and Pitch Orientation Relationships in the Gieon Meterorite, Acta Mat. 53 (2005) 1179-1190

11- Y. He, S. Godet, P. J. Jacques, and J.J. Jonas, Crystallographic Relations between Face- and Body-centered Cubic Crystals Formed Under Near-equilibrium Conditions: Observations From the Gibeon Meteorite, Acta Mat. 54 (2006) 1323-1334

12- A. Lambert-Perlade, A.F. Gourgues, A. Pineau, Austenite to Bainite Phase Transformation in the Heat Affected Zone of a High Strength Low Alloy Steel, Acta Mater. 52 (2004) 2337-2347

13- C. Cayron, ARPGE: a computer Program to Automatically Reconstruct the Parent Grains from Electron Backscattered Diffraction Data, J. Appl. Cryst. 40 (2007) 1183-1188

14- H. K. D. H. Bhadeshia, Bainite in Steels, Institute of Materials Pub., March 2001, 2nd ed., pp. 35-42

15- L. Wei, Investigating Correlations of Microstructures, Mechanical Properties and FSW Process Variables in Friction Stir Welded HSLA-65 Steel, PhD Dissertation, Brigham Young University, 2009

16- B.L. Adams, S.R. Kalidindi, D.T. Fullwood, Microstructure Sensitive Design for Performance Optimization, pp. 23-29, BYU Academic Publishing, Printed September 2006

17- R.S. Mishra, M.W. Mahoney, Friction Stir Welding and Processing, ASM International, 1st Ed., 2007

18- D. Lohwasser, Z. Chen, Friction Stir Welding- From Basics to Applications, Woodhead Pub. and CRC Press, 1st Ed., 2010

19- H. Fujii, L. Cui, N. Tsuji, M. Maeda, K. Nakata, K. Nogi, R. Ikeda, Friction Stir Welding of Carbon Steels, Materials Science and Engineering A 429 (2006) 50-57

20- H. Fujii, R. Ueji, R. Cui, K. Nakata, K. Nogi, Friction Stir Welding of Ultrafine Grained IF and Carbon Steels, Transactions of JWRI 35 (2006) No.1 47-52

21- T.W. Nelson, J. Su, R.J. Steel, Friction Stir Welding of Ferritic Steels, Proceedings of ISOPE-2004: 14th (2004) International Offshore and Polar Engineering Conference 2004

22- M. Posada, J. DeLoach, A.P. Reynolds, R. Fonda, J. Halpin, Evaluation of Friction Stir Welded HSLA-65, 4th International Friction Stir Welding Symposium, Park City UT, USA

23- P.J. Konkol, J.A. Mathers, R. Johnson, J.R. Pickerns, Friction Stir Welding of HSLA-65 Steel for Shipbuilding, J. of Ship Production 19 (2003) No.3 159-164

24- Z. Feng, M.L. Santella, S.A. David, R.J. Steel and S.M. Packer, T. Pan, M. Kuo, R.S. Bhantnagar, Friction Stir Spot Welding of Advanced High-Strength Steel-A Feasibility Study, SAE Transactions 114 (2005) 952-958

25- T.W. Nelson, L. Wei, M. Abbasi, Quantifying Post-Weld Microstructures in FSW HSLA-65, TMS 138th Annual Meeting, Feb. 2009, San Francisco, CA

26- L. Wei, Investigating Correlations of Microstructures, Mechanical Properties and FSW Process Variables in Friction Stir Welded High Strength Low Alloy 65 Steel, PhD Dissertation, Brigham Young University, 2009

27- D.P. Field, T.W. Nelson, Y. Hovanski, and K.V. Jata, Heterogeneity of Crystallographic Texture in Friction Stir Welds of Aluminum, Met. and Mat. Trans. A, V. 32A, Nov. 2001—2869

28- Y.S. Sato, H. Kokawa, K. Ikeda, M. Enomoto, S. Jogan, and T. Hashimoto, Microtexture in the Friction-Stir Weld of an Aliminum Alloy, Met. and Mat. Trans., Apr. 2001, 32A, 4, 941-948

29- B.D. Nelson, Using Design of Experiments and Electron Backscatter Diffraction to Model Extended Plasticity Mechanisms in Friction Stir Welded AISI 304L Stainless Steel, Unpublished Master's thesis, Brigham Young University

30- S. Mironov, Y.S. Sato, H. Kokawa, Microstructural Evolution During Friction Stir-Processing of Pure Iron, Acta Mat., 56 (2008), 2602-2614

31- L. Kestens, J. Jonas, Transformation and Recrystallization Textures Associated with Steel Processing, ASM Handbook Vol. 14A, 685-699

32- F. Montheillet, M. Cohen, and J.J. Jonas, Axial Stresses and Texture Development During the Torsion Testing of Al, Cu, and α-Fe, Acta Mat., Vol. 32, Issues 11, November 1984, Pages 2077-2089

33- S. Li, I.J. Beyerlein, M.A.M. Bourke, Texture Formation during Equal Channel Extrusion of FCC and BCC Materials: Comparison with Simple Shear, Mat. Sci. & Eng. A 394 (2005) 66-77

34- H. Beladi, P. Cizek, and P.D. Hodgson, Texture and Substructure Characteristics of Dynamic Recrystallization in a Ni-30%Fe Austenitic Model Alloy, Scripta Mat. 61 (2009) 528-531

35- P. Cizek, B.P Wynne, and W.M. Rainforth, EBSD Investigation of the Microstructure and Texture Characteristics of Hot Deformed Duplex Stainless Steel, J. of Microscopy, Vol. 222, Pt 2 May 2006, pp. 85-96

36- H. MIYAJI, E. FURUBAYASHI, Effect of Stress on the Variant Selection in Martensitic Transformation, Textures and Microstructures, 1991, Vols 14-18, pp. 561-566.

37- S.H. Lee, J. Kang, H.N. Han, K.H. Oh, H. Lee, D. Suh, S. Kim, Variant Selection in Mechanically-Induced Martensitic Transformation of Metastable Austenitic Steel, ISIJ Intl., Vol. 45 (2005), No. 8, pp. 1217-1219

38- P.S. Bate, W.B. Hutchinson, Imposed stress and variant selection: the role of symmetry and initial texture, J. Appl. Cryst. (2008). 41, 210–213

39- M. Humbert, B. Gardiola, C. Esling, G. Flemming, K.E. Hensger, Modelling of the variant selection mechanism in the phase transformation of HSLA steel produced by compact trip production, Acta Materialia 50 (2002) 1741–1747

40- M. Humbert, B. Petit, B. Bolle, and N. Gey, Analysis of the γ-ε-α' Variant Slection Induced by 10% Plastic Deformation in 304 Stainless Steel at -60 °C, Mat. Sci. Eng. A 454-455 (2007) 508-517.

41- A. Matsuzaki, H.K.D.H. Bhadeshia, and H. Harada, Stress affected bainitic transformation in a Fe-C-Si-Mn alloy, Acta Metall. Mater. Vol. 42, No. 4, pp. 1081-1090, 1994.

42- M. Karlsen, O. Grong, M. Sofferud, J. Hjelen, G. Rorvik, and R. Chiron, Scanning Electron Microscopy/Electron Backscatter Diffraction–Based Observations of Martensite Variant Selection and Slip Plane Activity in Supermartensitic Stainless Steels during Plastic Deformation at Elevated, Ambient, and Subzero Temperatures, Met. Mat. Trans. A, 40A, Feb. 2009—310-320

43- N. J. WITTRIDGE and J. J. JONAS, The austenite-to-martensite transformation in Fe–30%Ni after deformation by simple shear, Acta mater. 48 (2000) 2737-2749

44- T. Tomida, M. Wakita, M. Yoshida, N. Imai, Quantitative Prediction of Transformation Texture In Hot-Rolled Steel Sheets by Multiple KS Relation, Materials Processing and Texture, Edited by A.D. Rollett, Ceramic Transactions Vol. 200, 2009, Weily Pub., pp. 325-332

45- I. Charit, R.S. Mishra, Abnormal Grain Growth in Friction Stir Processed Alloys, Scripta Mater. 58 (2008) 367-371.

46- H.K.D.H. Bhadeshia, and R.W.K. Honeycombe, Steels-Microstructure and Properties, 3rd ed., 2006, BH Pub., pp. 42-44

47- H.K.D.H. Bhadeshia, Bainite in Steels- Transformation, Microstructure, and Properties, 2nd ed., 2001, IOM Com. Ltd., pp. 129-142.

48- B.L. Adams, S. Ta'Asan, D. Kinderlehrer, I. Livshits, D.E. Mason, Chun-te Wu, W.W. Mullins, G.R. Rohrer, A.D. Rollet, D.M. Saylor, Extracting Grain Boundary and Surface Energy from Measurement of Triple Junction Geometry, Interface Sci. 7, 321-338 (1999).

49- V. Randle, The Coincidence Site Lattice and 'Sigma Enigma', Mat. Char. 47 (2001) 411-416.

50- D. Wolf, Structure-Energy Correlation for Grain Boundaries in F.C.C. Metals-III. Symmetrical Tilt Boundaries, Acta Met. et Mat. Vol. 38 No. 5 pp.781-790, 1990.

51- G. Wang, V. Vitek, Relationships between Grain Boundary and Structure and Energy, Acta Met. Vol. 34, No. 5, pp. 951-960, 1986.

52- M. McLean, Grain-boundary Energy of Copper at 1030 °C, J. of Mat. Sci. B, (1973) 571-576.

53- T. Skidmore, R.G. Buchheit, M.C. Juhas, Grain Boundary Energy vs. Misorientation in Inconel 600 Alloy as Measured by Thermal Groove and OIM Analysis Correlation, Scripta Mater. 50 (2004) 873-877

54- D.W. Kim, D. Suh, R.S. Qin, and H.K.D.H. Bhadeshia, Dual orientation and variant selection during diffusional transformation of austenite to allotriomorphic ferrite, J. Mater. Sci. (2010) 45:4126–4132

APPENDIX A. FERRITE TO AUSTENITE ORIENTATION RECOVERY CODE

```
close all; clear all;

%Specify number of variant matrices
NumVariants = 24;

%input: two sets of Euler angles EA1 = [phi1 PHI phi2];
EA1 = [0 0 0];
EA2 = [0 0 0];

DataPoints = [EA1 ; EA2];

display('Reading in Austenite rotations')
%Form the 24 possible prior austenite g matrices
% for k = 1:NumVariants
%
%     startpt = ['S' num2str(4*(k-1)+3)];
%     endpt = ['U' num2str(4*(k-1)+5)];
%     GTransf(k,1:3,1:3) = xlsread('KS-NW.xls', 4, [startpt ':' endpt]);
% end
% save GTransfFerToAust GTransf
load GTransfFerToAust

display('Rotating')

%Now rotate each OIM point's g matrix by the NumVariants transformation
matrices
gAust(1:2,1:NumVariants,1:3,1:3) = 0;

for j = 1:2
    for k = 1:NumVariants
        gtrans(1:3,1:3) = GTransf(k,:,:);
        goim(1:3,1:3) =
euler2gmat(DataPoints(j,1),DataPoints(j,2),DataPoints(j,3));
        gAust(j, k, 1:3, 1:3) = gtrans*goim;
        if j == 1
            [p1(k), P(k), p2(k)]=gmat2euler(gtrans*goim);
            y(k) = 0;
            x(k) = k-1;
        else
            [p1(k+NumVariants), P(k+NumVariants),
p2(k+NumVariants)]=gmat2euler(gtrans*goim);
            y(k + NumVariants) = 1;
            x(k + NumVariants) = k-1;
        end
    end
end
filename = 'FerToAustCompare.ang';
WriteAngFile(p1,P,p2,x,y,filename);
```

```
%P1 rows, P2 columns
for P1ind = 1:NumVariants
    for P2ind = 1:NumVariants
        P1(1:3,1:3) = gAust(1,P1ind,:,:);
        P2(1:3,1:3) = gAust(2,P2ind,:,:);
        [angle(P1ind,P2ind),Axis,deltaG]=GeneralMisoCalc(P1,P2);
    end
end

figure; surf([1:NumVariants],[1:NumVariants],angle); shading interp
xlabel('Point 1 Austenite Variants');
ylabel('Point 2 Austenite Variants');
zlabel('Misorientation (degree)');

%Find points with misorientation below a certain angle
[p1set, p2set, angleset] = find(angle < 0.84);

%Get g-matrices of the combinations that are below the cutoff angle
for k = 1:length(p1set)

    gP1(1:3,1:3) = gAust(1,p1set(k),:,:);
    gP2(1:3,1:3) = gAust(2,p2set(k),:,:);
    [phi1, PHI, phi2]=gmat2euler(gP1)
    % ComboData(k).P1VarNum = p1set(k);
    % ComboData(k).P2VarNum = p2set(k);
    % ComboData(k).EA1 = [phi1, PHI, phi2];
    [phiii1, PHIII, phiii2]=gmat2euler(gP2)
    % ComboData(k).EA2 = [phi1, PHI, phi2];
    % ComboData(k).Angle = angle(p1set(k),p2set(k));
end
```